On Modeling and Control of a Holonomic Tricopter

Michalis Ramp[1] · Evangelos Papadopoulos[1]

Abstract

Most holonomic Unmanned Aerial Vehicles (HUAVs) (usually small-scale), employ at least four high-power thrusting actuators, resulting in increased mass, inertia, and energy consumption. In this work, a novel design for a HUAV using only three high-power thrusting actuators is developed. The pointing dynamics of the high rpm motor-propeller assemblies are included in the analysis, resulting in the exposure of oscillatory gyroscopic dynamics. These are studied analytically to yield vectoring oscillation frequency estimates, useful in selecting actuators. A geometric, singularity free, control framework comprised of a new control-allocation scheme and a new vectoring controller is developed. Stability proofs are included and controller robustness is addressed. Simulations (MATLAB/GAZEBO) demonstrating the effectiveness of the developed design and control framework are provided; a HUAV with independent position/attitude regulation (full pose control) using only three thrusting actuators is showcased.

Nomenclature

✉ Michalis Ramp
rampmich@central.ntua.gr

✉ Evangelos Papadopoulos
egpapado@central.ntua.gr

[1] School of Mechanical Engineering: Ethniko Metsovio Polytechneio Schole Mechanologon Mechanikon, National Technical University of Athens, Athens Greece

$\mathscr{I}_I\{\mathbf{E}_1, \mathbf{E}_2, \mathbf{E}_3\}$	Inertial reference frame.
$\mathscr{I}_i\{{}^i\mathbf{e}_1, {}^i\mathbf{e}_2, {}^i\mathbf{e}_3\}$	i^{th} body-fixed frame, $i = 0,...,3$.
$m_j \in \mathbb{R}^+$	mass of body $j = 0, ..., 3$, [kg]
${}^k\mathbf{J}_j \in \mathbb{R}^{3\times3}$	inertia of body $j = 0, ..., 3$, [kg m²]
${}^k\mathbf{x}_j \in \mathbb{R}^3$	position of jth body, $j = 0,...,3$, [m]
${}^k\mathbf{v}_j \in \mathbb{R}^3$	velocity of jth body, $j = 0,...,3$, [m s⁻¹]
${}^k\mathbf{r}_j \in \mathbb{R}^3$	vector from center of mass (CM) of body-0 to the extremity of Leg j, $j = 1, 2, 3$, [m]
${}^k\mathbf{p}_j \in \mathbb{R}^3$	vector ($\|{}^k\mathbf{p}_j\| = b$, $b \in \mathbb{R}^+$) from CM of body-j to the extremity of Leg j, $j = 1, 2, 3$, [m]

${}^I\mathbf{R}_i \in SO(3)$	linear transformation of the representation of a vector from $\mathscr{I}_i$, $i = 0, ..., 3$, to $\mathscr{I}_I$. Usage example: ${}^i\mathbf{R}_0 = {}^I\mathbf{R}_i^T {}^I\mathbf{R}_0 = {}^i\mathbf{R}_I {}^I\mathbf{R}_0$
${}^I\mathbf{R}_i^{i_d} \in SO(3)$	desired *absolute* attitude trajectory corresponding to body-i, $i = 0, .., 3$. Usage example: ${}^I\mathbf{R}_0^{i_d} = {}^I\mathbf{R}_i^{i_d}{}^i\mathbf{R}_0$
${}^k\boldsymbol{\omega}_j \in \mathbb{R}^3$	angular velocity of the, j^{th} body, $j = 0, ..., 3$, wrt., $\mathscr{I}_I$, [rad s⁻¹]
${}^k\boldsymbol{\omega}_{i_d/0} \in \mathbb{R}^3$	desired relative angular velocity of the, i^{th} body, $i = 1, ..., 3$, wrt., $\mathscr{I}_0$, [rad s⁻¹]
${}^k\boldsymbol{\omega}_{j/0} \in \mathbb{R}^3$	relative angular velocity of the, j^{th} body, $j = 1, ..., 3$, wrt., $\mathscr{I}_0$, [rad s⁻¹]
${}^k\mathbf{q}_j \in \mathbb{R}^3$	unit vector collinear to the jth propeller axis equal to ${}^k\mathbf{R}_j{}^j\mathbf{e}_3$
${}^k\mathbf{q}_{j_d} \in \mathbb{R}^3$	desired j^{th} propeller axis pointing direction equal to ${}^k\mathbf{R}_j^{j_d}{}^j\mathbf{e}_3$
$\phi, \theta, \Psi \in \mathbb{R}$	precession, nutation, spin Euler angles, of the "313" set, [rad]
$\mathbf{h} \in \mathbb{R}^3$	"321" Euler angles set, i.e., h_1=yaw, h_2=pitch, h_3=roll, [rad]
$b_m \in \mathbb{R}^+$	propeller torque constant, [m]
$b_T \in \mathbb{R}^+$	propeller thrust constant, [N s² rad⁻²]

$b \in \mathbb{R}^+$ distance from CM of body-j to the extremity of Leg j ($\|^k\mathbf{p}_j\| = b$), $j = 1, 2, 3$, [m]

$g \in \mathbb{R}^+$ gravity constant, 9.8 [m s^{-2}]

$\rho \in \mathbb{R}^+$ air density constant, [kg m^{-3}]

$^k\mathbf{g}_j \in \mathbb{R}^3$ gravity force of body $j = 0, ..., 3$, [N]

$^k\mathbf{u}_j \in \mathbb{R}^3$ control moment acting on body $j = 1, 2, 3$, [Nm]

$^k\mathbf{f}_{c,j} \in \mathbb{R}^3$ constraint force acting on body $j = 1, 2, 3$ by body 0, [N]

$^k\mathbf{f}_{p,j} \in \mathbb{R}^3$ propeller force acting on body $j = 1, 2, 3$, [N]

$^k\mathbf{f}_{p,j_e} \in \mathbb{R}^3$ relative thrust tracking error of the, j^{th} body, wrt., $\mathscr{I}_0$, [N]

$^k\mathbf{f}_{w,j} \in \mathbb{R}^3$ wind disturbance force applied on body $j = 0, ..., 3$, [N]

$^k\mathbf{n}_{w,j} \in \mathbb{R}^3$ wind disturbance moment applied on body $j = 0, ..., 3$, [Nm]

Subscript

Left superscript $^k(.)$ vector/matrix (.) expressed in frame $\mathscr{I}_k$, $k = I, 0, ..., 3$.

Right subscript $(.)_j$ j^{th} tricopter body, $j = 0, ..., 3$

Right subscript $(.)_d$ desired vector/matrix/signal

Right subscript $(.)_u$ signal resulting from control action

1 Introduction

Small-scale Unmanned Aerial Vehicles (UAVs), have attracted strong attention, by both the research community and industry. High demand for UAV civilian, scientific, and defense applications, is mainly attributed to their vertical take-off/landing and hover capabilities. Key examples include vehicles utilizing three [1, 2], four [3] or six [4] thrusting motors. UAVs are further classified as nonholonomic and holonomic vehicles.

Nonholonomic UAVs (such as quadrotors [5–7]) must lean their body sideways to change their horizontal position. This leaning motion restricts their ability to assume the required attitude when negotiating cluttered spaces or when performing complex surveillance/inspection or interaction tasks.

On the other hand, holonomic UAVs (HUAVs) can regulate their attitude and position independently [8–21]; they can naturally accomplish inspection, surveillance, mapping, or wrench application tasks. To advance their capabilities and produce efficient HUAVs, research focuses on full pose (position-attitude) control designs including quadrotors with tilting propellers [8–10], hexarotor designs

with canted propellers [11–14], or on a configuration where each propeller has a fixed orientation that is rotated about two possible axes with respect to the body-fixed frame [15, 16]. Unconventional designs include a UAV actuated by six optimally distributed rotors driven by reversible Electronic Speed Controllers (ESC) [17], a platform using seven thrusters with fixed orientations [18], a vehicle of eight rotors pairwise aligned with four different planes and driven by reversible ESCs [19], a holonomic UAV able to perform docking [20], and a UAV employing eight ducted-fans and 8 servos [21]. In most works, four high-power thrusting actuators or more are employed, resulting in HUAVs of increased mass/inertia and energy consumption.

This work presents a novel three-thruster HUAV, that operates by pointing its three rotors. A design of fully vectored rotors is chosen under the rationale that full maneuverability is maintained in any orientation, since the propellers are able to orient themselves and naturally resist external wrenches. In our prior work, a vectoring controller and the HUAV concept were introduced in [22, 23]. However the system studied in [22] was very simple, i.e., a single rigid body connected to a fixed base (the controller was unsuitable for the floating base architecture of the vehicle). The work in [23] represented an incomplete attempt since the control solution was developed under the hard limitation of internal wrench feedback availability; however, this required feedback sensors and therefore, it was not implementable.

This paper builds on our previous work and addresses the limitations of [22, 23], by developing a novel control framework. Although in most works the dynamics of reorienting fast spinning motor-propeller assemblies are ignored (the fast spinning motor-propeller assemblies are considered simply as sources of thrust and torque), here they are taken into consideration, exposing high-frequency oscillatory gyroscopic dynamics. The contributions of this work are the following; (i) an analytic expression for estimating the oscillatory gyroscopic dynamics frequency is developed, useful in selecting actuators. (ii) A new geometric controller to regulate the attitude of the high rotating speed motor-propeller assemblies is developed, for a floating base architecture. (iii) A new control-allocation solution is developed also taking into account the dynamics of the high rotating speed motor-propeller assemblies. This control solution is robust to parametric uncertainties, signal noise/estimation accuracy, and external disturbances. (iv) Stability assurances of the proposed control solution are produced via Lyapunov analysis. Simulation results in MATLAB and ROS/GAZEBO using a detailed system model demonstrate independent position/attitude regulation using three thrusting actuators only, proving the effectiveness of the developed approach.

2 Dynamics

2.1 Preliminaries

The holonomic tricopter design developed includes three motors vectored by two actuators each. The three motor-propeller assemblies are located at the extremities of the vehicle's legs (see Fig. 1); each mounted via a gimbal mechanism equipped with slip rings allowing unconstrained vectoring (3 thrust inputs + 6 gimbal inputs, i.e., 2 gimbal inputs for each thrust input). The legs are co-planar and are distributed evenly at 120° apart. Realistic vehicle parameters are obtained via a CAD design that includes all mechanical components (gimbals, servos, legs, etc.) and all electronics (battery, reversible ESCs, encoders, cameras, etc.), see Fig. 1.

The modeling of the platform was conducted in [23], but for completeness reasons it is presented briefly, here too. The HUAV is modeled as a four rigid body system. Body-0 (see Fig. 1) contains the frame, electronics, the gimbal mechanisms, and the static components of the motors. The gimbal mechanisms are included as part of Body-0 due to their small inertia; it is also assumed that vectoring is done at slow speeds. Body-i (i=1,2,3, see Fig. 1) is comprised by the spinning motor-propeller components of the assembly, and is called a thrusting assembly (TA). This modeling choice allows the study of gyroscopic dynamic phenomena, and leads to improved control design, and to vectoring actuator selection.

An inertial frame $\mathscr{I}_I\{\mathbf{E}_1, \mathbf{E}_2, \mathbf{E}_3\}$ and a body-0 fixed frame $\mathscr{I}_0\{^0\mathbf{e}_1, ^0\mathbf{e}_2, ^0\mathbf{e}_3\}$ at the center of mass (CM) of body-0 are used, see Fig. 1. Body-i fixed frames, $\mathscr{I}_i\{^i\mathbf{e}_1, ^i\mathbf{e}_2, ^i\mathbf{e}_3\}$, are also defined with $i = 1,2,3$ denoting the ith frame, see Fig. 1. The HUAV configuration is determined by the location of its body-0 CM, $^I\mathbf{x}_0$, and
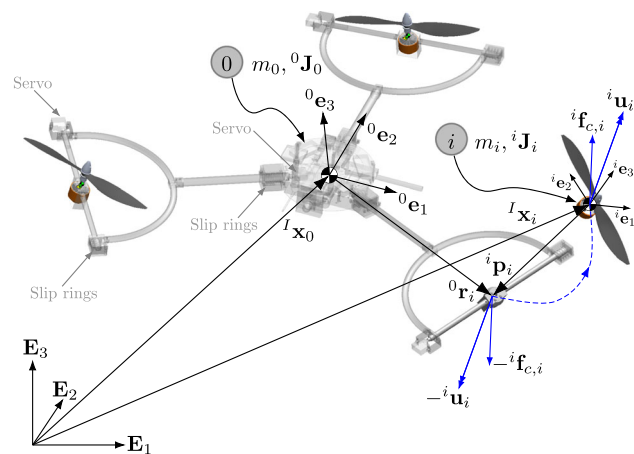

Fig. 1 Holonomic Tricopter design. Interaction wrench, $[^i\mathbf{f}_{c,i}; ^i\mathbf{u}_i]$, between body-0 and i^{th} thrust apparatus (TA) is also visible by exploding the ith-TA assembly

by its attitude, described by rotation matrix, $^I\mathbf{R}_0$, together with the attitude of the three TA's, $^I\mathbf{R}_i$, i=1,2,3. The HUAV configuration manifold is given by SE(3) × SO(3) × SO(3) × SO(3). During operation, each TA follows a desired pointing direction, and simultaneously tracks a desired angular velocity about the pointing direction, thus generating a force $^i\mathbf{f}_{p,i}$ [24] and a torque $^i\mathbf{n}_{p,i}$ [25]. Each TA is controlled by a moment $^i\mathbf{u}_i = [^iu_{i_1}; ^iu_{i_2}; ^iu_{i_3}]$. Components $^iu_{i_1}$, $^iu_{i_2}$ are responsible for pointing the ith-TA and are applied by the gimbal actuators; $^iu_{i_3}$ corresponds to the motor torque required for developing a desired propeller speed.

2.2 Equations of Motion (EoM)

The Newton-Euler methodology is employed in the derivation of the EoM. The position of the CM of the ith-TA, $^I\mathbf{x}_i$, (see Fig. 1) is given by

$$^I\mathbf{x}_i = {}^I\mathbf{x}_0 + {}^I\mathbf{R}_0 {}^0\mathbf{r}_i - {}^I\mathbf{R}_i {}^i\mathbf{p}_i$$

The ith-TA dynamics are described by

$$^I\dot{\mathbf{x}}_i = {}^I\mathbf{v}_i \tag{1a}$$

$$m_i {}^I\dot{\mathbf{v}}_i = {}^I\mathbf{g}_i + {}^I\mathbf{R}_i({}^i\mathbf{f}_{c,i} + {}^i\mathbf{f}_{p,i}) + {}^I\mathbf{f}_{w,i} \tag{1b}$$

$$^i\mathbf{J}_i {}^i\dot{\boldsymbol{\omega}}_i = {}^i\mathbf{u}_i + S\left({}^i\mathbf{p}_i\right){}^i\mathbf{f}_{c,i} + {}^i\mathbf{n}_{p,i} + {}^i\mathbf{n}_{w,i} - S\left({}^i\boldsymbol{\omega}_i\right){}^i\mathbf{J}_i {}^i\boldsymbol{\omega}_i \tag{1c}$$

$$^I\dot{\mathbf{R}}_i = {}^I\mathbf{R}_i S\left({}^i\boldsymbol{\omega}_i\right) \tag{1d}$$

where $^i\mathbf{f}_{p,i}$ ($^i\mathbf{n}_{p,i}$) is the thrust force (propeller torque) generated by the ith-TA propeller, $^i\mathbf{f}_{c,i}$ is the internal constraint force applied on the ith-TA by body-0, and $^I\mathbf{f}_{w,i}$ ($^i\mathbf{n}_{w,i}$) is the wind and aerodynamic disturbance force (torque). The cross product map $S(.)$: $\mathbb{R}^3 \to \mathfrak{so}(3)$, its inverse, $S^{-1}(.)$: $\mathfrak{so}(3) \to \mathbb{R}^3$, and the accelerations, are given in the Appendix, see Eqs. (A1), (A2b). The thrust force, $^i\mathbf{f}_{p,i}$, (propeller torque, $^i\mathbf{n}_{p,i}$) is

$$^i\mathbf{f}_{p,i} = \left[0; 0; b_T \left({}^i\boldsymbol{\omega}_i^{T\,i}\mathbf{e}_3\right)^2\right] \tag{2a}$$

$$^i\mathbf{n}_{p,i} = -b_m \,\text{sgn}\left({}^i\boldsymbol{\omega}_i^{T\,i}\mathbf{e}_3\right){}^i\mathbf{f}_{p,i} \tag{2b}$$

where sgn(.) is the sign function. Using Eq. (1b), the internal constraint force applied on the ith-TA, $^i\mathbf{f}_{c,i}$, by body-0 is

$$^i\mathbf{f}_{c,i} = {}^i\mathbf{R}_I \left(m_i {}^I\dot{\mathbf{v}}_i - {}^I\mathbf{g}_i - {}^I\mathbf{f}_{w,i}\right) - {}^i\mathbf{f}_{p,i} \tag{3}$$

The angular velocity of the ith-TA, $^i\boldsymbol{\omega}_i = [^i\omega_{i_1}; ^i\omega_{i_2}; ^i\omega_{i_3}]$, can be expressed as

$$^i\boldsymbol{\omega}_i = {}^i\boldsymbol{\omega}_0 + {}^i\boldsymbol{\omega}_{i/0} = {}^i\mathbf{R}_0 {}^0\boldsymbol{\omega}_0 + {}^i\boldsymbol{\omega}_{i/0} \tag{4}$$

where $^i\boldsymbol{\omega}_{i/0}$ is the angular velocity of the ith-TA with respect to body-0. The angular acceleration of the ith-TA,

$^i\dot{\boldsymbol{\omega}}_i = \left[^i\dot{\omega}_{i_1}; \, ^i\dot{\omega}_{i_2}; \, ^i\dot{\omega}_{i_3}\right]$, is found by differentiating Eq. (4), yielding

$$^i\dot{\boldsymbol{\omega}}_i = \, ^i\mathbf{R}_0 \, ^0\dot{\boldsymbol{\omega}}_0 - S\left(^i\boldsymbol{\omega}_{i/0}\right) \, ^i\mathbf{R}_0 \, ^0\boldsymbol{\omega}_0 + \, ^i\dot{\boldsymbol{\omega}}_{i/0} \tag{5}$$

Body-0 accelerates under the action of the forces $-^i\mathbf{f}_{c,i}$ applied by the ith-TA (given by Eq. (3)) and the body-0 gravity force, $^I\mathbf{g}_0$. Attitude-wise, each TA applies a moment $-^i\mathbf{u}_i$, on body-0. Thus, the body-0 EoM are given by

$$^I\dot{\mathbf{x}}_0 = \, ^I\mathbf{v}_0 \tag{6a}$$

$$m_0 \, ^I\dot{\mathbf{v}}_0 = \, ^I\mathbf{g}_0 - \sum_{i=1}^{3} \, ^I\mathbf{R}_i \, ^i\mathbf{f}_{c,i} + \, ^I\mathbf{f}_{w,0} \tag{6b}$$

$$^0\mathbf{J}_0 \, ^0\dot{\boldsymbol{\omega}}_0 = \sum_{i=1}^{3} S\left(^0\mathbf{r}_i\right)\left(^0\mathbf{R}_i\left(-^i\mathbf{f}_{c,i}\right)\right) + \, ^0\mathbf{n}_{w,0}$$
$$- \sum_{i=1}^{3}\left(^0\mathbf{R}_i \, ^i\mathbf{u}_i\right) - S\left(^0\boldsymbol{\omega}_0\right) \, ^0\mathbf{J}_0 \, ^0\boldsymbol{\omega}_0 \tag{6c}$$

$$^I\dot{\mathbf{R}}_0 = \, ^I\mathbf{R}_0 S\left(^0\boldsymbol{\omega}_0\right) \tag{6d}$$

The forces/moments $^I\mathbf{f}_{w,i}, \, ^i\mathbf{n}_{w,i}, \, i = 0, .., 3$ in Eqs. (1) and (6), due to the wind and other disturbances are modeled as in [26] and assumed to be bounded

$$\|^I\mathbf{f}_{w,i}(t)\| \le f_{w,i_{max}}, i = 0, .., 3, \forall t \tag{7a}$$

$$\|^i\mathbf{n}_{w,i}(t)\| \le n_{w,i_{max}}, i = 0, .., 3, \forall t \tag{7b}$$

The system inputs are the moments $^i\mathbf{u}_i$ (i=1,2,3) actuating each TA. The EoM of the entire UAV are given by Eqs. (1b)-(1d), (6b)-(6d); an alternative form of the EoM containing all states and control inputs is found by rewriting the EoM in matrix form with respect to $\left[^I\dot{\mathbf{v}}_0, \, ^0\dot{\boldsymbol{\omega}}_0, \, ^1\dot{\boldsymbol{\omega}}_1, \, ^2\dot{\boldsymbol{\omega}}_2, \, ^3\dot{\boldsymbol{\omega}}_3\right]^T$ as follows

$$\mathbf{M}\begin{bmatrix} ^I\dot{\mathbf{v}}_0 \\ ^0\dot{\boldsymbol{\omega}}_0 \\ ^1\dot{\boldsymbol{\omega}}_1 \\ ^2\dot{\boldsymbol{\omega}}_2 \\ ^3\dot{\boldsymbol{\omega}}_3 \end{bmatrix} + \boldsymbol{\Gamma} + \mathbf{G} + \mathbf{P} + \mathbf{D} = \mathbf{B}\begin{bmatrix} ^1\mathbf{u}_1 \\ ^2\mathbf{u}_2 \\ ^3\mathbf{u}_3 \end{bmatrix} \tag{8}$$

where $\mathbf{M} \in \mathbb{R}^{15\times15}$, $\boldsymbol{\Gamma}, \mathbf{G}, \mathbf{P}, \mathbf{D} \in \mathbb{R}^{15\times1}$ and $\mathbf{B} \in \mathbb{R}^{15\times9}$ are given in the Appendix, see Eqs. (A3)-(A9a).

2.3 Relative Motion of the ith Thrusting Assembly wrt. Body-0

The dynamics governing the relative motion of the ith-TA wrt. body-0 are employed in the control design. Noting that $^I\mathbf{R}_i = \, ^I\mathbf{R}_0 \, ^0\mathbf{R}_i$, the relative motion dynamics are derived by substituting Eqs. (3) and (A2b) in (1c), and then by inserting Eq. (5) into the resulting expression. This yields

the dynamics of the relative motion of the ith-TA with respect to body-0 as

$$^i\boldsymbol{\mathcal{J}}_i \, ^i\dot{\boldsymbol{\omega}}_{i/0} = S\left(^i\mathbf{p}_i\right) m_i \, ^i\dot{\mathbf{v}}_0 + \, ^i\mathbf{Z}_i \, ^0\dot{\boldsymbol{\omega}}_0 + \, ^i\mathbf{n}_{r,i}$$
$$+ S\left(^i\mathbf{p}_i\right)\left(-^i\mathbf{f}_{w,i}\right) + \, ^i\mathbf{n}_{w,i} + \, ^i\mathbf{u}_i \tag{9a}$$

$$^0\dot{\mathbf{R}}_i = \, ^0\mathbf{R}_i S\left(^i\boldsymbol{\omega}_{i/0}\right) \tag{9b}$$

where $^i\mathbf{n}_{r,i} \in \mathbb{R}^{3\times1}$, and $^i\boldsymbol{\mathcal{J}}_i, \, ^i\mathbf{Z}_i \in \mathbb{R}^{3\times3}$ containing inertia terms, are given in the Appendix by Eqs. (A10a)-(A10d).

3 Pointing an Outrunner Motor-Propeller Assembly

The dynamic phenomena that occur during flight by pointing a high angular speed motor-propeller are studied using a simple motor-propeller assembly (i^{th}-TA) that is pointed with respect to a fixed base, see Fig. 2. To simplify the notation, the body-0 fixed frame $\mathscr{I}_0$ is used as the global reference and the CM of the ith-TA is connected to $\mathscr{I}_0$ by the vector $^i\mathbf{p}_i$

$$^i\mathbf{p}_i = -b \, ^i\mathbf{e}_3, \, b \in \mathbb{R}^+ \tag{10}$$

The origin of the ith-TA fixed frame $\mathscr{I}_i$ coincides with the CM of the ith-TA, see Fig. 2. Writing the system angular momentum balance with respect to the origin of $\mathscr{I}_0$, and calculating its derivative we get

$$^i\mathbf{u}_i = \, ^i\mathbf{J}_i \, ^i\dot{\boldsymbol{\omega}}_i + S\left(^i\boldsymbol{\omega}_i\right) \, ^i\mathbf{J}_i \, ^i\boldsymbol{\omega}_i$$
$$+ m_i S\left(^i\mathbf{p}_i\right)\left\{S\left(^i\boldsymbol{\omega}_i\right) S\left(^i\boldsymbol{\omega}_i\right) \, ^i\mathbf{p}_i + S(^i\dot{\boldsymbol{\omega}}_i) \, ^i\mathbf{p}_i\right\} \tag{11}$$

Assuming that $^i\mathbf{J}_i = \text{diag}\left(^iJ_{i_{1,1}}, \, ^iJ_{i_{2,2}}, \, ^iJ_{i_{3,3}}\right)$, then Eq. (11) in component form is given by

$$^iu_{i_1} = \left(^iJ_{i_{3,3}} - \, ^iJ_{i_{2,2}} - m_ib^2\right) \, ^i\omega_{i_3} \, ^i\omega_{i_2} + \left(^iJ_{i_{1,1}} + m_ib^2\right) \, ^i\dot{\omega}_{i_1} \tag{12a}$$

$$^iu_{i_2} = \left(^iJ_{i_{1,1}} - \, ^iJ_{i_{3,3}} + m_ib^2\right) \, ^i\omega_{i_3} \, ^i\omega_{i_1} + \left(^iJ_{i_{2,2}} + m_ib^2\right) \, ^i\dot{\omega}_{i_2} \tag{12b}$$

$$^iu_{i_3} = \left(^iJ_{i_{2,2}} - \, ^iJ_{i_{1,1}}\right) \, ^i\omega_{i_2} \, ^i\omega_{i_1} + \, ^iJ_{i_{3,3}} \, ^i\dot{\omega}_{i_3} \tag{12c}$$
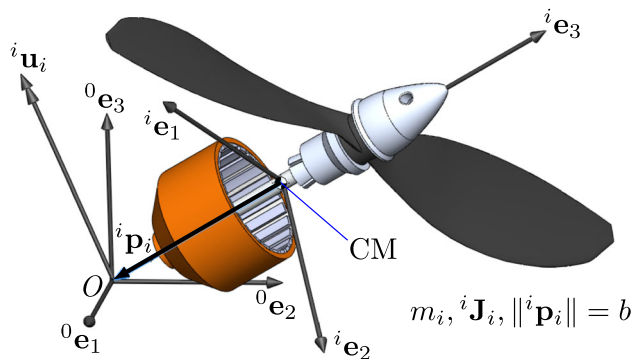

Fig. 2 Free body diagram of the ith-TA, modeled as a rigid body

The controlled motion of this system is characterized by nutation and precession oscillations [27]. Nutation is described by a change in the second Euler angle of the "313" sequence, denoted here by θ_i; it is a swaying/nodding motion of the pointing axis, $^i\mathbf{e}_3$, with respect to $^0\mathbf{e}_3$. Precession describes the azimuth variation of the assembly's pointing axis, $^i\mathbf{e}_3$, about $^0\mathbf{e}_3$. It is described by a change in the first Euler angle of the "313" sequence, denoted here by ϕ_i [28]. The dynamics of this system are studied aiming to obtain analytic expressions for the nutation/precession frequencies.

Assuming a model-based control input, $^i\mathbf{u}_i(t)$, that achieves smooth pointing trajectory of constant high propeller speed, $^i\omega_{i_3} \gg {^i\omega_{i_1}}, {^i\omega_{i_2}}$, Eqs. (12a), (12b) are solved for the controlled angular rates $^i\omega_{i_{1u}}$, $^i\omega_{i_{2u}}$ (subscript "u" denotes that the angular rates are due to the applied control $^i\mathbf{u}_i(t)$). These are given by

$$
\begin{aligned}
^i\omega_{i_{1u}} &= \frac{^iu_{i_2}(t) - \left(^iJ_{i_{2,2}} + m_ib^2\right)^i\dot{\omega}_{i_2}}{\left(^iJ_{i_{1,1}} - {^iJ_{i_{3,3}}} + m_ib^2\right)^i\omega_{i_{3u}}}, \\
^i\omega_{i_{2u}} &= \frac{^iu_{i_1}(t) - \left(^iJ_{i_{1,1}} + m_ib^2\right)^i\dot{\omega}_{i_1}}{\left(^iJ_{i_{3,3}} - {^iJ_{i_{2,2}}} - m_ib^2\right)^i\omega_{i_{3u}}}
\end{aligned}
\tag{13}
$$

The equations reveal linear dependence of the angular rates to the angular accelerations of the neighboring axes (the pointing axis is excluded). This indicates that movement about axis $^i\mathbf{e}_1$ produces motion about axis $^i\mathbf{e}_2$ and vice versa.

3.1 Nutation/Precession Frequency Estimation

To extract the nutation and precession responses from $^i\boldsymbol{\omega}_i$, the Euler angle succession "313" that describes these motions [28] is used

$$
\begin{bmatrix} \dot{\phi}_i \\ \dot{\theta}_i \\ \dot{\psi}_i \end{bmatrix} = \begin{bmatrix} \frac{\sin(\psi_i)}{\sin(\theta_i)} & \frac{\cos(\psi_i)}{\sin(\theta_i)} & 0 \\ \cos(\psi_i) & -\sin(\psi_i) & 0 \\ -\frac{\sin(\psi_i)\cos(\theta_i)}{\sin(\theta_i)} & -\frac{\cos(\psi_i)\cos(\theta_i)}{\sin(\theta_i)} & 1 \end{bmatrix} \begin{bmatrix} ^i\omega_{i_{1u}} \\ ^i\omega_{i_{2u}} \\ ^i\omega_{i_{3u}} \end{bmatrix}
\tag{14}
$$

where ψ_i is the third Euler angle of the "313" succession; it denotes the rotation angle of the motor-propeller assembly about its own axis $^i\mathbf{e}_3$.

Note that Eq. (14) is valid only when $\theta_i \notin \{n\pi | n \in \mathbb{N}\}$ and this agrees with the physical intuition that no precession exists when the motor-propeller axis of rotation (AoR) is aligned with the precession AoR. However, since we are working with coordinate-free representations of attitude in the modeling, control design and simulation, we are not restricted by any specific attitude or Euler angle limitation. Additionally, Eq. (14) is not used during vehicle operation/control, it is rather used as an aid in understanding the behavior of the gyroscopic phenomena.

Taking into account the high-velocity spin of the assembly, the fact that the assembly has small inertia, and

the form of Eq. (14), low amplitude but high-frequency oscillations on the nutation/precession rates, $\dot{\theta}_i/\dot{\phi}_i$, are expected. The low amplitude is due to to the smooth pointing motion i.e., small $^i\omega_{i_{1u}}$, $^i\omega_{i_{2u}}$, while the high-frequency is due to the high $^i\omega_{i_{3u}}$ that makes ψ_i to increase continually. Hence, ψ_i trigonometric functions affecting Eq. (14), oscillate between -1 to 1 very fast. Moreover, the faster the propeller spin, the faster will be the interchange of the effect of $^i\omega_{i_{1u}}$, $^i\omega_{i_{2u}}$ on the nutation/precession rates, $\dot{\theta}_i/\dot{\phi}_i$.

An estimate of the high-frequency oscillations can be obtained by approximating the value of ψ_i as follows: Solving Eq. (14) for $^i\omega_{i_{3u}}$, noting that $\dot{\psi}_i \gg \dot{\phi}_i$, and considering the boundedness of the trigonometric numbers then, $^i\omega_{i_{3u}} \approx \dot{\psi}_i$. Hence

$$
\psi_i(t) \approx {^i\omega_{i_{3u}}} t + \psi_i(0), \ \forall t \geq 0
\tag{15}
$$

Using Eqs. (13) into (14), the nutation rate of change, $\dot{\theta}_i$, is given by

$$
\begin{aligned}
\dot{\theta}_i = {} & \cos(\psi_i)\frac{^iu_{i_2} - \left(^iJ_{i_{2,2}} + m_ib^2\right)^i\dot{\omega}_{i_2}}{\left(^iJ_{i_{1,1}} - {^iJ_{i_{3,3}}} + m_ib^2\right)^i\omega_{i_{3u}}} \\
& -\sin(\psi_i)\frac{^iu_{i_1} - \left(^iJ_{i_{1,1}} + m_ib^2\right)^i\dot{\omega}_{i_1}}{\left(^iJ_{i_{3,3}} - {^iJ_{i_{2,2}}} - m_ib^2\right)^i\omega_{i_{3u}}}
\end{aligned}
\tag{16}
$$

The hypothesis that the control achieves smooth pointing of the TA assembly, allows one to assume that $^iu_{i_1}(t)$, $^iu_{i_2}(t)$, will have an oscillatory nature to counteract the ψ_i dependent trigonometric terms. Hence, $^iu_{i_1}(t)$, $^iu_{i_2}(t)$, must contain ψ_i dependent trigonometric terms as follows

$$
^iu_1(t) = \eta_{i_1}(\alpha_{i_1}(t)\sin(\psi_i) + \beta_{i_1}(t)\cos(\psi_i)) + \left(^iJ_{i_{1,1}} + m_ib^2\right)^i\dot{\omega}_{i_1} \tag{17a}
$$

$$
^iu_2(t) = \eta_{i_2}(\alpha_{i_2}(t)\sin(\psi_i) + \beta_{i_2}(t)\cos(\psi_i)) + \left(^iJ_{i_{2,2}} + m_ib^2\right)^i\dot{\omega}_{i_2} \tag{17b}
$$

$$
\eta_{i_1} = \left(^iJ_{i_{3,3}} - {^iJ_{i_{2,2}}} - m_ib^2\right)^i\omega_{i_3} \tag{17c}
$$

$$
\eta_{i_2} = \left(^iJ_{i_{1,1}} - {^iJ_{i_{3,3}}} - m_ib^2\right)^i\omega_{i_3} \tag{17d}
$$

where $\alpha_{i_j}(t)$, $\beta_{i_j}(t) \in \mathbb{R}$ are the control amplitudes needed to achieve the desired pointing trajectory. Substituting Eqs. (17) in (16), and applying trigonometric identities, the nutation rate, $\dot{\theta}_i$, is approximated by

$$
\begin{aligned}
\dot{\theta}_i \approx {} & \frac{1}{2}\Big(\alpha_{i_2}(t)\sin(2\psi_i) + \beta_{i_2}(t)(1 + \cos(2\psi_i)) \\
& -\alpha_{i_1}(t)(1 - \cos(2\psi_i)) - \beta_{i_1}(t)\sin(2\psi_i)\Big)
\end{aligned}
\tag{18}
$$

Equation (18) indicates that the frequency of the oscillatory behavior is described by the argument of the trigonometric functions, namely $2\psi_i$. Using this result and Eq. (15), the nutation frequency, $f_\sim$, is found as

$$
(2\pi f_\sim)t + \text{phase} = 2\psi_i \cong 2\left(^i\omega_{i_{3u}}t + \psi_i(0)\right) \Rightarrow
$$

$$
f_\sim(t) \cong {^i\boldsymbol{\omega}_{3u}}(t)/\pi \tag{19}
$$

By repeating the above analysis using the precession component of Eq. (14), it can be shown that the same result holds for the precession rate, $\dot{\phi}_i$. Hence Eq. (19) holds for both nutation and precession frequencies. Thus in experimental pointing implementations, Eq. (19), allows easy calculation of the gyroscopic oscillation frequencies useful in evaluating or selecting of pointing actuators.

Equation (19), is verified via a simulation involving the vectoring tricopter UAV performing a 90° pitch attitude maneuver while hovering still. The simulation conditions and system parameters are given in Section 5, Table 1 and Eq. (48). Each TA approximately follows a desired pointing trajectory of a pure 90° rotation about the $^0\mathbf{e}_1$ body fixed axis with a steady spin velocity. The results are presented in Fig. 3 and in the supplementary video file (second flight scenario).

After an initial position deviation (see $\|\mathbf{e}_x\|$ in Fig. 3a), a smooth steady hover (position hold) and transition to the desired orientation is observed (see Fig. 3a). Yaw and roll angles stay close to zero and are omitted in Fig. 3a. The 2nd-TA motion is displayed in Fig. 3b-d. The TA orientation relative to body-0 is varied by 90°, while the propellers constantly point upward to maintain the desired gravity-canceling position (see ϕ_2, θ_2 in Fig. 3b). The propeller velocity, $\dot{\psi}_2$, is maintained close to 748.2 rad/s despite some variations due to the vehicle body-0 changing orientation and the disturbances (Fig. 3b). The vectoring control effort

required is less than 0.5 [Nm] (see $^2u_{2_1}$, $^2u_{2_2}$ in Fig. 3d). The control that actuates the spin of the propeller, $^2u_{2_3}$, modulates due to the disturbances (Fig. 3d).

The nutation rate, $\dot{\theta}_2(t)$ (extracted using Eq. (14)) shows high frequency gyroscopic oscillations (see $\dot{\theta}_2$ in Fig. 3c). An FFT analysis of the signal (see PSD in Fig. 3c) reveals a low frequency group of less than 5 Hz, a group with a central frequency at 235.5 Hz, and a group with a central frequency at 474.6 Hz. The low frequency group is attributed to the desired maneuver and the disturbances. The higher frequency groups are attributed to gyroscopic oscillations where the group with a central frequency at 235.5 Hz is the base frequency of the gyroscopic oscillations. The last group is considered a higher harmonic of the base frequency since $2 \times 235.5 \approx 474.6$ Hz. Using the developed estimate, Eq. (19), we compute the nutation frequency as 236.80 Hz, i.e., with a deviation equal to 0.55 %. The same holds for the precession rate (omitted due to space limitations), validating the developed result.

Concluding, by studying the pointing motion of a high RPM motor/propeller assembly and by using the "313" Euler angle succession the high frequency precession/nutation oscillations were calculated analytically (Eq. (19)). This equation can be employed in the process of selecting actuators and allows the swift discern of the gyroscopic oscillation frequencies and the nature of the

Fig. 3 UAV position hold with 90° pitch maneuver. (3a) Top: Position error (norm). Middle: Pitch maneuver attitude response (Blue: state, Black: desired). Bottom: Initial pose (left) vs. final pose (right) of the UAV. (3b) 2nd-TA attitude relative to $\mathcal{I}_I$. Top: Precession $\phi_2(t)$. Middle: Nutation $\theta_2(t)$. Bottom: Spin/propeller rate $\dot{\psi}_2(t)$. (3c) 2nd-TA nutation rate response. Top: Nutation rate $\dot{\theta}_2$. Middle: Detail of $\dot{\theta}_2$. Bottom: Nutation frequency content via FFT. (3d) 2nd-TA control torque, $^2\mathbf{u}_2$
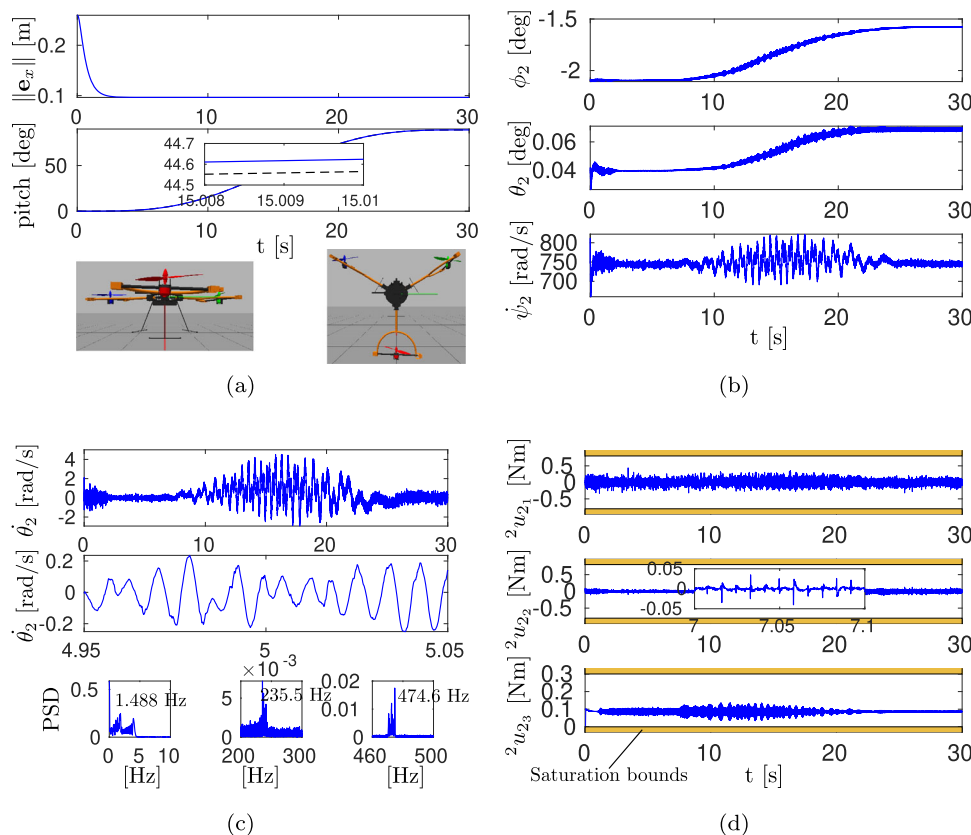
motion (without the need of time consuming simulations or experiments).

4 Control Design

For HUAVs, a global operational envelope is needed; hence a coordinate-free, i.e., geometric framework is employed to avoid singularities and ambiguities; also the resulting controller action belongs to the system nonlinear manifold.

The developed control strategy is summarized next; and illustrated in Fig. 4. Vehicle control is conducted in three steps: (a) an output tracking control law computes a virtual-desired wrench, $\left[{}^I\mathbf{f}_0; {}^0\mathbf{n}_0\right]_d$, that minimizes the body-0 output tracking error (top left block of Fig. 4), (b) the desired wrench, is resolved into desired forces for the TA's; these are transformed to the needed desired pointing, ${}^0\mathbf{q}_{i_d}$, and angular velocity, ${}^i\boldsymbol{\omega}_{i_d/0}$, states for each TA (allocation block of Fig. 4), (c) the desired TA states are fed into vectoring controllers that apply the needed control torques, ${}^i\mathbf{u}_i$, on each TA producing the thrusts which achieve the desired vehicle pose (i^{th} vectoring block of Fig. 4).

In short the individual motor-propeller generated thrusts are considered as alternative control inputs in linearizing the control model; this is done by allocating the needed motor-propeller pointing directions, ${}^0\mathbf{q}_{i_d}$, and angular velocities, ${}^i\boldsymbol{\omega}_{i_d/0}$, via a simple geometric rule.

4.1 Vectoring Controller

The control design procedure begins with the development of the vectoring controller that actuates each TA. Unit vectors, ${}^0\mathbf{q}_i$, ($i = 1, 2, 3$) collinear to the ith-propeller axis are defined as the system pointing states; a singularity-free pointing attitude representation. The propeller axis vector, ${}^0\mathbf{q}_i$, and angular velocity, ${}^i\boldsymbol{\omega}_{i/0}$, relative to the body-0 frame i.e. the TA states, and their derivatives are given by

$$ {}^0\mathbf{q}_i = {}^0\mathbf{R}_i {}^i\mathbf{e}_3 \tag{20a} $$

$$ {}^0\dot{\mathbf{q}}_i = S\left({}^0\mathbf{R}_i {}^i\boldsymbol{\omega}_{i/0}\right) {}^0\mathbf{q}_i \tag{20b} $$

$$ {}^i\boldsymbol{\omega}_{i/0} = {}^i\boldsymbol{\omega}_i - {}^i\mathbf{R}_0 {}^0\boldsymbol{\omega}_0 \tag{20c} $$

$$ {}^i\dot{\boldsymbol{\omega}}_{i/0} = -{}^i\mathbf{R}_0 {}^0\dot{\boldsymbol{\omega}}_0 + S\left({}^i\boldsymbol{\omega}_{i/0}\right){}^i\mathbf{R}_0 {}^0\boldsymbol{\omega}_0 + {}^i\dot{\boldsymbol{\omega}}_i \tag{20d} $$

Hence, the ith-TA configuration manifold with respect to body-0 is given by $S^2 \times \mathbb{R}^3$, i.e. a vector on $S^2 = \left\{\boldsymbol{\xi} \in \mathbb{R}^3 \mid \boldsymbol{\xi}^T\boldsymbol{\xi} = 1\right\}$ denoting the pointing state, and a vector on $\mathbb{R}^3$ denoting the TA angular velocity.

For the desired body-i *absolute* attitude trajectory ${}^I\mathbf{R}_i^{i_d} \in$ SO(3), the following kinematic relation holds

$$ {}^I\dot{\mathbf{R}}_i^{i_d} = {}^I\mathbf{R}_i^{i_d} S\left({}^i\boldsymbol{\omega}_{i_d}\right), i = 0, .., 3 \tag{21} $$

where ${}^i\boldsymbol{\omega}_{i_d} \in \mathbb{R}^3$ is the desired angular velocity of body-i, $i = 0, .., 3$. Using ${}^0\mathbf{R}_i^{i_d} = {}^0\mathbf{R}_I {}^I\mathbf{R}_i^{i_d}$, the desired pointing direction, ${}^0\mathbf{q}_{i_d}$, its derivative, ${}^0\dot{\mathbf{q}}_{i_d}$, the desired angular velocity relative to $\mathscr{I}_0$, ${}^i\boldsymbol{\omega}_{i_d/0}$, and its acceleration, ${}^i\dot{\boldsymbol{\omega}}_{i_d/0}$, are found as

$$ {}^0\mathbf{q}_{i_d} = {}^0\mathbf{R}_i^{i_d} {}^i\mathbf{e}_3 = {}^0\mathbf{R}_I {}^I\mathbf{q}_{i_d} \tag{22a} $$

$$ {}^0\dot{\mathbf{q}}_{i_d} = S\left({}^0\mathbf{R}_i^{i_d} {}^i\boldsymbol{\omega}_{i_d/0}\right) {}^0\mathbf{q}_{i_d} \tag{22b} $$

$$ {}^i\boldsymbol{\omega}_{i_d/0} = {}^i\boldsymbol{\omega}_{i_d} - {}^i\mathbf{R}_0^{i_d} {}^0\boldsymbol{\omega}_0 \tag{22c} $$

$$ {}^i\dot{\boldsymbol{\omega}}_{i_d/0} = {}^i\dot{\boldsymbol{\omega}}_{i_d} - {}^i\mathbf{R}_0^{i_d} {}^0\dot{\boldsymbol{\omega}}_0 + S\left({}^i\boldsymbol{\omega}_{i_d/0}\right){}^i\mathbf{R}_0^{i_d} {}^0\boldsymbol{\omega}_0 \tag{22d} $$

The above desired states are provided via control allocation. Suitable tracking errors are needed that employ the developed pointing state vectors $\left({}^0\mathbf{q}_i, {}^i\boldsymbol{\omega}_{i/0}\right)$ and desired vectors $\left({}^0\mathbf{q}_{i_d}, {}^i\boldsymbol{\omega}_{i_d/0}\right)$. The error function, Ψ_i, [29, 38]

$$ \Psi_i = 1 - {}^0\mathbf{q}_i^T {}^0\mathbf{q}_{i_d} \tag{23} $$

is used that quantifies the pointing attitude error. When the unit vectors, ${}^0\mathbf{q}_i, {}^0\mathbf{q}_{i_d}$, are antipodal, $\Psi_i = 2$, i.e. $\Psi_{i_\%} = 100\%$ attitude error. If ${}^0\mathbf{q}_i, {}^0\mathbf{q}_{i_d}$ are perpendicular, $\Psi_i = 1$, and when ${}^0\mathbf{q}_i, {}^0\mathbf{q}_{i_d}$, are coincident, $\Psi_i = 0$, i.e. $\Psi_{i_\%} = 0\%$ error. The pointing error vector, ${}^i\mathbf{e}_{q,i}$, and angular velocity error vector, ${}^i\mathbf{e}_{\omega,i}$, are derived via Eq. (23) and are given by [22, 23]

$$ {}^i\mathbf{e}_{q,i} = {}^i\mathbf{R}_0 S\left({}^0\mathbf{q}_{i_d}\right) {}^0\mathbf{q}_i \tag{24a} $$

$$ {}^i\mathbf{e}_{\omega,i} = {}^i\boldsymbol{\omega}_{i/0} - {}^i\mathbf{R}_0 {}^0\mathbf{R}_i^{i_d} {}^i\boldsymbol{\omega}_{i_d/0} \tag{24b} $$

Fig. 4 High level tricopter control strategy
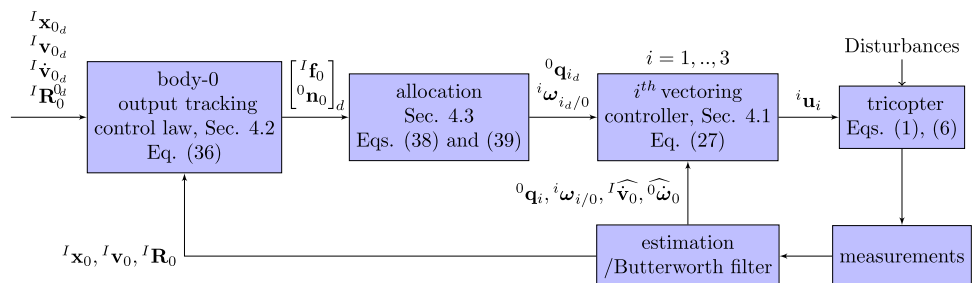
A necessary condition in using Eq. (24a), is that $\Psi_i\left({}^0\mathbf{q}_{i_d}, {}^0\mathbf{q}_i\right) < 2$ i.e., ${}^0\mathbf{q}_{i_d} \neq -{}^0\mathbf{q}_i$. Also via Eq. (24a), the following bounding inequality holds [22, 23]

$$
\forall \psi_i \in \mathbb{R}^+ | \Psi_i \leq \psi_i < 2 \implies
$$
$$
\frac{1}{2}\|{}^i\mathbf{e}_{q,i}\|^2 \leq \Psi_i \leq \frac{1}{2-\psi_i}\|{}^i\mathbf{e}_{q,i}\|^2 \tag{25}
$$

Using Eqs. (20b), (22b), and (23), the error dynamics are found to be

$$
\dot{\Psi}_i = \left({}^0\mathbf{R}_i\,{}^i\mathbf{e}_{q,i}\right)^T {}^0\mathbf{R}_i\,{}^i\mathbf{e}_{\omega,i} \tag{26a}
$$
$$
{}^i\dot{\mathbf{e}}_{q,i} = {}^i\mathcal{E}_i\,{}^i\mathbf{e}_{\omega,i} \tag{26b}
$$
$$
{}^i\dot{\mathbf{e}}_{\omega,i} = {}^i\dot{\boldsymbol{\omega}}_{i/0} + {}^i\mathbf{a}_i \tag{26c}
$$

where ${}^i\mathcal{E}_i \in \mathbb{R}^{3\times3}$ and ${}^i\mathbf{a}_i \in \mathbb{R}^3$ are given by

$$
{}^i\mathcal{E}_i = {}^i\mathbf{R}_0\left({}^0\mathbf{q}_{i_d}^T {}^0\mathbf{q}_i\mathbf{1} - {}^0\mathbf{q}_{i_d}\,{}^0\mathbf{q}_i^T\right){}^0\mathbf{R}_i \tag{27a}
$$
$$
{}^i\mathbf{a}_i = S\left({}^i\boldsymbol{\omega}_{i/0}\right){}^i\mathbf{R}_0\,{}^0\mathbf{R}_i^{i_d}\,{}^i\boldsymbol{\omega}_{i_d/0} - {}^i\mathbf{R}_0\,{}^0\mathbf{R}_i^{i_d}\,{}^i\dot{\boldsymbol{\omega}}_{i_d/0} \tag{27b}
$$
$$
= -S\left({}^i\mathbf{R}_0\,{}^0\mathbf{R}_i^{i_d}\,{}^i\boldsymbol{\omega}_{i_d/0}\right){}^i\mathbf{e}_{\omega,i} - {}^i\mathbf{R}_0\,{}^0\mathbf{R}_i^{i_d}\,{}^i\dot{\boldsymbol{\omega}}_{i_d/0} \tag{27c}
$$

The developed vectoring controller, ${}^i\mathbf{u}_i$, stabilizing the ith-TA dynamics, Eq.(9), was developed via the Lyapunov analysis in Appendix B, and is given by

$$
{}^i\mathbf{u}_i = -\widehat{{}^i\mathbf{n}_{r,i}} - S\left({}^i\mathbf{p}_i\right)m_i\,\widehat{{}^i\dot{\mathbf{v}}_0} - \widehat{{}^i\mathbf{Z}_i\,{}^0\dot{\boldsymbol{\omega}}_0}
$$
$$
+ k_\omega^{-1}\widehat{{}^i\boldsymbol{\mathcal{J}}_i}\left(-k_\omega\,{}^i\mathbf{a}_i - (k_q + \Psi_i){}^i\mathbf{e}_{q,i} - \dot{\Psi}_i\,{}^i\mathbf{e}_{q,i} - \gamma\,{}^i\mathbf{s}_i\right) \tag{28a}
$$
$$
{}^i\mathbf{s}_i = (k_q + \Psi_i){}^i\mathbf{e}_{q,i} + k_\omega\,{}^i\mathbf{e}_{\omega,i}, \ \ k_q, k_\omega \in \mathbb{R}^+ \tag{28b}
$$
$$
\gamma = \gamma_1 + \gamma_2 + \gamma_3, \gamma_3 = \gamma_4 + \gamma_5, \gamma_{i=1,\dots,5} \in \mathbb{R}^+ \tag{28c}
$$
$$
\gamma_5 > N_{\omega,i_{max}}/\lambda_{\mathcal{J}_i} \tag{28d}
$$
$$
k_\omega > N_{n,i_{max}}/\left(\gamma_5\lambda_{\mathcal{J}_i} - N_{\omega,i_{max}}\right) \tag{28e}
$$
$$
\gamma_4 > \left(\gamma_5\Psi_i^2\right)/\left((k_q + \Psi_i)^2 - \Psi_i^2\right) \tag{28f}
$$
$$
\lambda_{\mathcal{J}_i} = \lambda_{min}\left({}^i\boldsymbol{\mathcal{J}}_i^{-1}\widehat{{}^i\boldsymbol{\mathcal{J}}_i}\right) \tag{28g}
$$

where the bounds $N_{n,i_{max}}, N_{\omega,i_{max}}$, which depend on the desired trajectory, are given in Appendix B, Eq. (B9), $\lambda_{min}(.)$ denotes the smallest eigenvalue of the term (.), and $\widehat{(.)}$ denotes an estimate of the term (.). Vector ${}^i\mathbf{p}_i$, is given by Eq. (10). Matrices ${}^i\boldsymbol{\mathcal{J}}_i$, $\widehat{{}^i\boldsymbol{\mathcal{J}}_i}$ given in Appendix A, Eq. (A10a) are diagonal positive definite matrices since ${}^i\mathbf{J}_i$, $\widehat{{}^i\mathbf{J}}_i$ (used in Eq. (A10a)) are positive definite also. The values of $\lambda_{\mathcal{J}_i}$, and $\Delta\mathcal{J}_i$ are needed in the calculation of γ, k_ω. To do so, knowledge of ${}^i\boldsymbol{\mathcal{J}}_i^{-1}\widehat{{}^i\boldsymbol{\mathcal{J}}_i}$ is required; this is done using a conservative estimate of ${}^i\boldsymbol{\mathcal{J}}_i^{-1}$ given by $(\iota\,\widehat{{}^i\boldsymbol{\mathcal{J}}_i})^{-1}$ where $\iota > 1$, and conservatively selecting larger gains than those instructed by Eqs. (28d), (28e).

The controller works as follows. The first three terms of Eq. (28a), are feedback linearizing terms. The term ${}^i\mathbf{a}_i$, cancels residual terms caused by the desired vectoring command. The term $(k_q + \Psi_i){}^i\dot{\mathbf{e}}_{q,i}$ penalizes the rate of

change of the pointing error, to smooth out the pointing response. Using Eq. (26a), the term $\dot{\Psi}_i\,{}^i\mathbf{e}_{q,i}$ is given by

$$
\dot{\Psi}_i\,{}^i\mathbf{e}_{q,i} = {}^i\mathbf{e}_{q,i}\,{}^i\mathbf{e}_{q,i}^T\,{}^i\mathbf{e}_{\omega,i} \tag{29}
$$

Hence, the term $\dot{\Psi}_i\,{}^i\mathbf{e}_{q,i}$ smooths out the response by penalizing the angular velocity error, ${}^i\mathbf{e}_{\omega,i}$, as a function of the ${}^i\mathbf{e}_{q,i}\,{}^i\mathbf{e}_{q,i}^T$ matrix. The vector ${}^i\mathbf{s}_i$, describes a nonlinear surface in the angular velocity error and the pointing tracking error space. The surface acts as a PD correction term; however the action of this surface is penalized by multiplying ${}^i\mathbf{s}_i$ by gain γ, thus allowing for fine tuning of the response (see [22] for details). The stability properties of the controller are provided in the following proposition.

Proposition 1 *Under the following conditions:*

1. *For bounded external disturbances as prescribed by Eq. (7)*

2. *A bounded desired angular velocity profile ${}^i\boldsymbol{\omega}_{i_d/0}(t) \in \mathbb{R}^3$ which is sufficiently smooth as defined by*

$$
\|{}^i\boldsymbol{\omega}_{i_d/0}(t)\| \leq {}^i\omega_{i_d/0_{max}}, \forall t \tag{30a}
$$
$$
\|{}^i\dot{\boldsymbol{\omega}}_{i_d/0}(t)\| \leq {}^i\dot{\omega}_{i_d/0_{max}}, \forall t \tag{30b}
$$

3. *A desired pointing direction ${}^0\mathbf{q}_{i_d}(t) \in S^2$ subject to Eq. (22b), that is never antipodal to ${}^0\mathbf{q}_i(t)$ as described by*

$$
\Psi_i\left({}^0\mathbf{q}_i(t), {}^0\mathbf{q}_{i_d}(t)\right) < 2, \forall t \tag{31}
$$

4. *Assuming a good estimate of body-0 acceleration and system parameters so that*

$$
\|{}^I\dot{\mathbf{v}}_0(t) - {}^I\widehat{\dot{\mathbf{v}}}_0(t)\| \leq e_{\dot{v}_{0_{max}}} \forall t \tag{32a}
$$
$$
\|{}^i\mathbf{Z}_i(t){}^0\dot{\boldsymbol{\omega}}_0(t) - {}^i\widehat{\mathbf{Z}}_i(t){}^0\widehat{\dot{\boldsymbol{\omega}}}_0(t)\| \leq e_{\dot{\omega}_{0_{max}}} \forall t \tag{32b}
$$
$$
\|{}^i\mathbf{n}_{r,i}(t) - {}^i\widehat{\mathbf{n}}_{r,i}(t)\| \leq e_{n_{r,i_{max}}} \forall t \tag{32c}
$$

5. *For a sufficiently large gain γ such that*

$$
\delta_i < \lambda_{min}(\boldsymbol{\Pi}_{3_i}) \tag{33}
$$

(for $\boldsymbol{\Pi}_{3_i} \in \mathbb{R}^{3\times3}$, δ_i and their γ dependence see Appendix B Eqs. (B11b), (B15b))

The developed controller given in Eq. (28a renders $\left({}^i\mathbf{e}_{q,i}, {}^i\mathbf{e}_{\omega,i}\right)$ uniformly ultimately bounded (UUB), stabilizing $\left({}^i\mathbf{e}_{q,i}, {}^i\mathbf{e}_{\omega,i}\right)$ exponentially in a bounded set of the zero equilibrium in the presence of parametric uncertainties, disturbances and signal estimation errors. An estimate of the ultimate bound is given by

$$
\|\mathbf{z}_i\| < \sqrt{\frac{\delta_i}{\lambda_{min}(\boldsymbol{\Pi}_{3_i})}}, \ \mathbf{z}_i = \left[\|{}^i\mathbf{e}_{q,i}\|; \|{}^i\mathbf{e}_{\omega,i}\|\right] \tag{34}
$$

Proof See Appendix B. $\qquad\square$

The developed controller architecture/design yields strong robustness properties in the presence of parametric uncertainties, disturbances and signal estimation errors. The components δ_i, $\boldsymbol{\Pi}_{3_i}$ (used in Eqs. (33), (34)) are composed by additional terms that are a function of the disturbances, the desired trajectory, the estimation errors and the gains. Proposition 1 implies that the lower the magnitude of the disturbances, the lesser the aggressiveness of the desired trajectory, the higher the accuracy of the estimation of the parameters/accelerations, and/or the higher the value of γ, the ultimate bound shrinks. Additionally, as γ is increased, the tracking errors converge faster to the set containing the desired equilibrium. Concluding, the developed controller is singularity-free, satisfying the design requirements.

An important ramification of Proposition 1 is that it proves that under the action of the controller, and the assumptions made, the vectoring states of each TA relative to body-0 are stabilized in a neighborhood of the desired equilibrium without assuming body-0 stability. Consequently the relative motion of each TA with respect to body-0 is stable and bounded. This result is needed to prove stability for the overall system.

4.2 Output Tracking Position-Attitude Control Law

A control law is designed accounting for the rigid body motion of each TA and generating a desired wrench command that allows the body-0 of the vehicle to track any sufficiently smooth pose trajectory. Due to the tilting of high rpm spinning rigid bodies, this is a difficult control problem; straight forward feedback linearization is insufficient and a combination of Lyapunov design techniques and partial feedback linearization is needed to produce a stable and robust control law.

The output tracking controller employs the attitude error function Ψ_0, [30]

$$\Psi_0 = 2 - \sqrt{1 + \mathrm{tr}\left[{}^0\mathbf{R}_I^{0_d}(t)\,{}^I\mathbf{R}_0(t)\right]} \qquad (35)$$

where tr[.] is the trace function; Eq. (35) compares the current attitude of body-0, ${}^I\mathbf{R}_0$, with the desired one, ${}^I\mathbf{R}_0^{0_d}$. The maximum attitude error occurs when the rotation matrices are antipodal ($\Psi_0 = 2$, $\Psi_{0_\%} = 100\,\%$). Via Ψ_0, the error vectors for attitude, $\mathbf{e}_R$, and angular velocity, $\mathbf{e}_\omega$, are produced, (see [30] for details) allowing the definition of the following pose error vectors

$$\mathbf{e}_{\mathbf{x},R} = \begin{bmatrix} \mathbf{e}_x \\ \mathbf{e}_R \end{bmatrix} = \begin{bmatrix} {}^I\mathbf{x}_0 - {}^I\mathbf{x}_{0_d} \\ \frac{1}{2}\frac{S^{-1}\left({}^0\mathbf{R}_I^{0_d}\,{}^I\mathbf{R}_0 - {}^0\mathbf{R}_I\,{}^I\mathbf{R}_0^{0_d}\right)}{\sqrt{1 + \mathrm{tr}[{}^0\mathbf{R}_I^{0_d}\,{}^I\mathbf{R}_0]}} \end{bmatrix} \qquad (36a)$$

$$\mathbf{e}_{\mathbf{v},\boldsymbol{\omega}} = \begin{bmatrix} \mathbf{e}_v \\ \mathbf{e}_\omega \end{bmatrix} = \begin{bmatrix} {}^I\mathbf{v}_0 - {}^I\mathbf{v}_{0_d} \\ {}^0\boldsymbol{\omega}_0 - {}^I\mathbf{R}_0^T\,{}^I\mathbf{R}_0^{0_d}\,{}^0\boldsymbol{\omega}_{0_d} \end{bmatrix} \qquad (36b)$$

A necessary condition in using the attitude error vector, $\mathbf{e}_R$, is that ${}^I\mathbf{R}_0^{0_d}$ is not antipodal to ${}^I\mathbf{R}_0$. This condition derives from the fact that the SO(3) topology prohibits the design of a smooth global controller [31].

The pose control law is developed by studying the structure of the dynamics of body-0. First Eqs. (6b)-(6c), are substituted in Eqs. (1b)-(1c). The obtained expression is solved for the body-0 resultant wrench; it is used in conjunction with partial feedback linearization techniques and guided by Lyapunov analysis on the combined closed-loop system dynamics until a control law satisfying all requirements is obtained.

Specifically it generates the desired wrench that must be applied by the combined action of the TA's on body-0 to achieve stable flight and is derived as

$$\begin{bmatrix} {}^I\mathbf{f}_0 \\ {}^0\mathbf{n}_0 \end{bmatrix}_d = \mathbf{h}_g - \mathbf{h}_p + \mathbf{C}\begin{bmatrix} K_v^{-1}\mathbf{1} & 0_{3\times 3} \\ 0_{3\times 3} & K_\Omega^{-1}\mathbf{1} \end{bmatrix}$$
$$\left\{-\zeta\mathbf{z} - \begin{bmatrix} -K_v{}^I\dot{\mathbf{v}}_{0_d} + K_x\mathbf{e}_v \\ K_\Omega{}^0\mathbf{a}_0 + (K_R + \Psi_0)\dot{\mathbf{e}}_R + \dot{\Psi}_0\mathbf{e}_R \end{bmatrix}\right\} \qquad (37a)$$
$$\zeta = \zeta_1 + \zeta_2 \qquad (37b)$$

where K_v, K_x, K_Ω, K_R, ζ_1, $\zeta_2 \in \mathbb{R}^+$. The vector $\mathbf{z} \in \mathbb{R}^{6\times 1}$ is defined as

$$\mathbf{z} = \begin{bmatrix} K_v\mathbf{e}_v + K_x\mathbf{e}_x \\ K_\Omega\mathbf{e}_\omega + (K_R + \Psi_0)\mathbf{e}_R \end{bmatrix} \qquad (38)$$

while the expressions for the terms $\mathbf{h}_g$, $\mathbf{h}_p \in \mathbb{R}^{6\times 1}$, $\mathbf{C} \in \mathbb{R}^{6\times 6}$, ${}^0\mathbf{a}_0$, $\dot{\mathbf{e}}_R \in \mathbb{R}^{3\times 1}$, $\dot{\Psi}_0 \in \mathbb{R}$ used in Eq. (37) are given in Appendix A, Eqs. (A13a)-(A17a); the stability proof is provided in Section 4.4, Proposition 2.

Depending on the desired pose trajectory, Eq. (37) may produce a non-realizable (due to actuator limits) wrench; this can be avoided by selecting a sufficiently smooth desired pose trajectory that respects these limitations. Guidelines on selecting a pose trajectory that comply to TA limitations are provided in Section 4.4.

4.3 Allocation

For this platform, allocation aims to achieve a minimum norm solution; such a solution implies energy conservation. A solution mapping the desired wrench, Eq. (37), into thrust commands for each TA is obtained as

$$\begin{bmatrix} \left({}^I\mathbf{R}_1{}^1\mathbf{f}_{p,1}\right)_d \\ \left({}^I\mathbf{R}_2{}^2\mathbf{f}_{p,2}\right)_d \\ \left({}^I\mathbf{R}_3{}^3\mathbf{f}_{p,3}\right)_d \end{bmatrix} = \mathbf{A}^\# \begin{bmatrix} {}^I\mathbf{f}_0 \\ {}^0\mathbf{n}_0 \end{bmatrix}_d \qquad (39)$$

The matrix $\mathbf{A} \in \mathbb{R}^{6\times 9}$ (see Appendix Eq. (A18)), defined by platform geometry, has full row rank; it is used to calculate the Moore-Penrose pseudoinverse given by $\mathbf{A}^\# = \mathbf{A}^T(\mathbf{A}\mathbf{A}^T)^{-1} \in \mathbb{R}^{9\times 6}$.

Using Eq. (39), the desired commands for the propeller direction, $^I\mathbf{q}_{i_d}$, and speed, $^i\omega_{i_d}$, are computed as follows

$$^I\mathbf{q}_{i_d} = \left(^I\mathbf{R}_i{}^i\mathbf{f}_{p,i}\right)_d / \left\|\left(^I\mathbf{R}_i{}^i\mathbf{f}_{p,i}\right)_d\right\| \tag{40a}$$

$$^i\omega_{i_d} = \sqrt{b_T^{-1}\|\left(^I\mathbf{R}_i{}^i\mathbf{f}_{p,i}\right)_d\|}{}^i\mathbf{e}_3 \tag{40b}$$

Via the vectoring controller, Eq. (28a), the TA dynamics in Eq. (1) track $\left(^I\mathbf{q}_{i_d},{}^i\omega_{i_d}\right)$ and produce the desired thrusts of Eq. (39) that linearize the dynamics and achieve the desired motion.

For proper generation of the desired commands, $\|\left(^I\mathbf{R}_i{}^i\mathbf{f}_{p,i}\right)_d\| \neq 0$ must hold. Since Eq. (39) is a function of the desired pose trajectory, if the trajectory is selected to be adequately smooth, then $\|\left(^I\mathbf{R}_i{}^i\mathbf{f}_{p,i}\right)_d\| \neq 0$ because the platform must compensate for gravity continuously. In the event that $\|\left(^I\mathbf{R}_i{}^i\mathbf{f}_{p,i}\right)_d\|=0$, for example if a free-fall command is issued, the propeller direction is selected as that of the previous time step, i.e., $^I\mathbf{q}_{i_d}(t) = {}^I\mathbf{q}_{i_d}(t-dt)$.

4.4 System Overall Stability

Under the assumption of body-0 known parameters, it is proved that the developed control solution yields stable platform motion/trajectory tracking. A hard requirement for the validity of the proof is that the body-0 desired attitude command lies in

$$L_2 = \left\{^I\mathbf{R}_0^{0_d} \in SO(3) \mid \Psi_0\left(^I\mathbf{R}_0, {}^I\mathbf{R}_0^{0_d}\right) < 2\right\} \tag{41}$$

i.e., the desired body-0 attitude, $^I\mathbf{R}_0^{0_d}$, is not antipodal to the current attitude, $^I\mathbf{R}_0$. Any antipodal physical attitude can be reached by any intermediate attitude step.

4.4.1 Note on the Vectoring Controller Stability

In Section 4.1 it was proved that the relative motion of each TA with respect to body-0 is stabilized in a neighborhood of the zero equilibrium, independently from the motion of body-0 with respect to the inertial frame (see proof of Proposition 1) and without assuming body-0 stability. Explicitly it was shown that the pointing error vectors, $^i\mathbf{e}_{q,i}$, $^i\mathbf{e}_{\omega,i}$ are UUB in the set L_σ^c, see Appendix B, Eq. (B19a). The implication is that there exist $\sigma_q, \sigma_\omega, \sigma_{\dot\omega} \in (0, \infty)$ such that

$$\|^0\mathbf{q}_i(t) - {}^0\mathbf{q}_{i_d}(t)\| < \sigma_q, t \to \infty \tag{42a}$$

$$\|^i\boldsymbol\omega_{i/0}(t) - {}^i\boldsymbol\omega_{i_d/0}(t)\| < \sigma_\omega, t \to \infty \tag{42b}$$

$$\|^i\dot{\boldsymbol\omega}_{i/0}(t) - {}^i\dot{\boldsymbol\omega}_{i_d/0}(t)\| < \sigma_{\dot\omega}, t \to \infty \tag{42c}$$

Equation (42), is used throughout the stability proof allowing to address, at selected instances, terms containing $^i\boldsymbol\omega_{i/0}$, $^i\dot{\boldsymbol\omega}_{i/0}$ as bounded disturbances.

The rational behind the system overall stability proof is that it sets the conditions/bounds for the disturbances,

the signal/parameter estimation errors and the pose tracking requirements (i.e. flight, vehicle and path planning conditions) at which the vectoring controller (Eq. 28a) can efficiently track the desired commands for the propeller direction, $^I\mathbf{q}_{i_d}$, and speed, $^i\omega_{i_d}$; they are generated by the output tracking position/attitude controller. Accurate tracking of the desired propeller direction/speed, $^I\mathbf{q}_{i_d}/{}^i\omega_{i_d}$, yields accurate desired thrust tracking (given in Eq. 39); this produces the needed desired wrench (Eq. 37) that acts on body-0 resulting in efficient pose tracking.

The proposition regarding platform stability is stated next.

Proposition 2 *Under the following conditions:*

1. *For a sufficiently smooth pose command,* $^I\mathbf{x}_{0_d}$, $^I\mathbf{R}_0^{0_d}$, *such that the control-allocation strategy given by Eqs. (37), (39), (40), yields TA commands,* $^I\mathbf{q}_{i_d}$, $^i\omega_{i_d}$, *that comply with the conditions of Proposition 1,*
2. *Under the conditions of Prop. 1 ensuring stable vectoring controller performance,*
3. *For a body-0 desired attitude,* $^I\mathbf{R}_0^{0_d}$, *that is never antipodal to* $^I\mathbf{R}_0$ *as described by Eq. (41),*
4. *For a sufficiently large gain* $\zeta = \zeta_1 + \zeta_2$ *such that*

$$\epsilon_{max} < \zeta_2\sqrt{2\lambda_{max}(\mathcal{W}_2)} \tag{43}$$

   (for ϵ_{max}, $\mathcal{W}_2$ *see Appendix C Eqs. (C10c), (C4c))*
5. *For known body-0 parameters,*

The control-allocation strategy given by Eqs. (37), (39), (40), through the action of the developed vectoring controller (see Eq. (28a), renders the tracking errors ($\mathbf{e}_x$, $\mathbf{e}_v$, $\mathbf{e}_R$, $\mathbf{e}_\omega$) of body-0 UUB; they are stabilized exponentially in a bounded set of the zero equilibrium in the presence of bounded external disturbances. An estimate of the ultimate bound is given by,

$$\|\mathbf{z}\| = \frac{\epsilon_{max}}{\zeta_2} \tag{44}$$

Proof See Appendix C. □

The components, ϵ_{max}, $\mathcal{W}_2$ (in Eqs. (43) and (44)), are functions of the disturbances, the TA thrust tracking errors, the relative motion between each TA and body-0, and the gains. To keep the proposition compact, the expressions for ϵ_{max}, $\mathcal{W}_2$ in Eq. 43 are given in Appendix C, Eqs. (C10c), (C4c).

The ultimate bound, i.e. Eq. (44), depends on the TA thrust tracking errors, the disturbances, and the relative motion between each TA and body-0; all are bounded. The ultimate bound shrinks with less aggressive desired trajectories of body-0 and smaller disturbances. This bound also depends on the gain ζ via ζ_2; a larger ζ yields a smaller

ultimate bound while the tracking errors converge faster to the desired equilibrium. However the value of ζ is limited by the actuator/thrust constraints. The assumption of body-0 parameter knowledge is reasonable since a high fidelity estimate can be obtained via a CAD software or standard system identification techniques.

Concluding, the developed control solution that yields the aforementioned overall system stability characteristics is composed by Eqs. (37), (39), (40), and (28a). In terms of sequence, first (i) Eq. (37) computes the desired wrench, $\left[{}^I\mathbf{f}_0 \ {}^0\mathbf{n}_0 \right]^T_d$, that needs to be applied on body-0 to minimize its output pose-tracking error, then (ii) Eq. (39) maps the desired wrench into thrust commands, $\left({}^I\mathbf{R}_i {}^i\mathbf{f}_{p,i} \right)_d$, for each of the three TAs (i=1,2,3), followed by (iii) Eq. (40) that transforms the thrust commands into desired commands for the propeller direction, ${}^I\mathbf{q}_{i_d}$, and speed, ${}^i\boldsymbol{\omega}_{i_d}$, of each TA, and finally (iv) Eq. (28a) that yields the control action, ${}^i\mathbf{u}_i$, applied on each TA, that produces the desired thrust commands and minimizes the pose-tracking error of body-0.

5 Simulation Results

The ability of the platform to achieve independent position-attitude regulation is illustrated through simulation results.

5.1 Simulation Set-Up

The experiments are conducted under the effect of actuator constraints, parametric uncertainties, signal noise, and disturbances.

5.1.1 Parameters and Gains

The system parameters (obtained by the CAD design of the platform, see Fig. 1) are given in Table 1. The mass of the motor-propeller assembly is 0.109[kg]; 0.049[kg] correspond to the rotating parts, 0.06[kg] to the stationary parts. The stationary masses are included in the mass of body-0. The controller parameters are given in Table 1; they were computed following the guidelines provided in [27]. The large pointing gains k_q, k_ω result from the fact that the desired TA angular velocity is very large combined with the fact that the TA inertia is very small.

5.1.2 Measurement Noise Modeling

Precision encoders measure each TA assembly's relative orientation with respect to body-0. An Inertial Measurment Unit (IMU) is available; together with a Kalman filter, they provide an estimate of the body-0 attitude. The IMU measurements are modeled as, [32]:

$$
{}^0\tilde{\boldsymbol{\omega}}_0 = {}^0\boldsymbol{\omega}_0 + {}^0\mathbf{n}_{\omega_0} + {}^0\mathbf{b}_{\omega_0}
$$
$$
{}^0\dot{\mathbf{b}}_{\omega_0} = {}^0\mathbf{n}_b
$$

where ${}^0\mathbf{b}_{\omega_0}$ is the gyroscope bias considered to be a "Wiener" process and the terms ${}^0\mathbf{n}_{\omega_0}$ and ${}^0\mathbf{n}_b$ represent white Gaussian noise with zero-mean and standard deviations σ_{ω_0} and σ_b, respectively. The simulated IMU is the ADIS16477 with an Angular Random Walk specification of

Table 1 System & Controller parameters

Type	Values
Kinematic parameters	${}^0\mathbf{r}_1 = [0.3352; -0.1935; 0]\,[m]$
	${}^0\mathbf{r}_2 = [-0.3352; -0.1935; 0]\,[m]$
	${}^0\mathbf{r}_3 = [0; 0.3870; 0]\,[m],\ b = 0\,[m]$
Inertial parameters	$m_0 = 1.5679\,[kg],\ m_i = 0.049\,[kg]$
	${}^0\mathbf{J}_0 = \begin{bmatrix} 0.04899 & 0 & 0 \\ 0 & 0.049804 & 0 \\ 0 & 0 & 0.10461 \end{bmatrix}\,[kg\,m^2]$
	${}^i\mathbf{J}_i = \begin{bmatrix} 7.8460 & -0.76200 & 0 \\ -0.76200 & 2.7490 & 0 \\ 0 & 0 & 5.7700 \end{bmatrix} 10^{-5}\,[kg\,m^2]$
TA coefficients	$b_T = 1.0122 \cdot 10^{-5}\,[N\,s^2/rad^2],\ b_m = 0.0154\,[m]$
Allocation gains	$K_x = 106.97,\ K_v = 20.68$
	$K_R = 204.08,\ K_\Omega = 28.57,\ \zeta = 2$
Vectoring gains	$k_q = 555516.78,\ k_\omega = 1788.79,\ \gamma = 310.55$

$0.3 [^o/\sqrt{hr}]$ and an In-Run Bias Stability of $2.5 [^o/hr]$ [33]. Noise is inserted into the measurements modeled by

$$^I\tilde{\mathbf{R}}_i = \exp(\mathrm{n}_{R_i}, \mathbf{t}_i)^I\mathbf{R}_i, i=0, .., 3 \tag{45}$$

where $^I\mathbf{R}_i$, is the true attitude, $\exp(\mathrm{n}_{R_i}, \mathbf{t}_i)$ is the exponential map given in Appendix Eq. (A19), $\mathbf{t}_i$ is the instantaneous axis of rotation of $^I\mathbf{R}_i$, and n_{R_i} represents Gaussian noise of zero-mean and standard deviations $\sigma_{R_0}=0.1582^o$ for body-0 (simulating Kalman filtering performance according to [34] at 200[Hz]), and $\sigma_{R_i}=0.087^o$ (simulating the pointing actuators homing offset documented in [35]), $i = 1, 2, 3$. Note that the signals $\widehat{^0\boldsymbol{\omega}_0}, \widehat{^0\dot{\boldsymbol{\omega}}_0}, \widehat{^I\mathbf{v}_0}, \widehat{^i\dot{\boldsymbol{\omega}}_{i_d}}, i = 1, 2, 3$ are filtered using a 2nd order low-pass Butterworth filter with a cutoff frequency of 25Hz.

5.1.3 Actuator Constraints

Actuator constraints in the form of saturation are placed on the control inputs based on the Dynamixel XL430-W250T actuator [35]. For $i = 1, 2, 3$ the control input $^i\mathbf{u}_i$ is limited as follows

$$\|^iu_{i_j}\| \le 0.8 \text{ [Nm]}, j = 1, 2 \tag{46a}$$
$$0 \le {}^iu_{i_3} \le 0.3 \text{ [Nm]} \tag{46b}$$

5.1.4 Wind Disturbance Modeling

A bounded disturbance wrench, $\left[{}^I\mathbf{f}_{w,i}; {}^i\mathbf{n}_{w,i}\right], i = 0, .., 3$ simulating the wind is applied using the wind profile shown in Fig. 5, in conjunction with the drag equation [36]. The
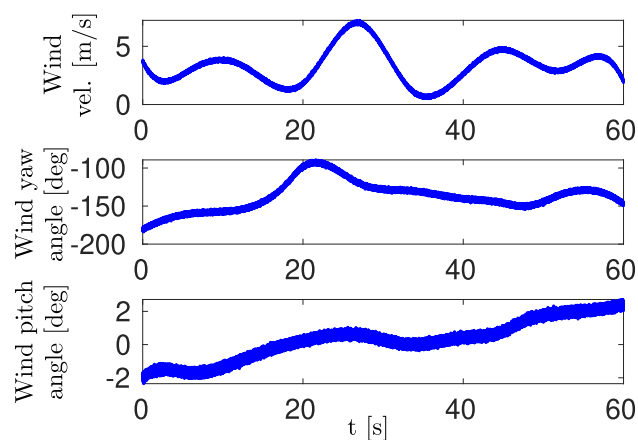

Fig. 5 Wind disturbance profile

drag coefficient, $\mathbf{C}_{D,0} \in \mathbb{R}^{3\times3}$, and reference area, $\mathbf{A}_{D,0} \in \mathbb{R}^{3\times3}$, matrices of the vehicle are given by,

$$\mathbf{C}_{D,0} = \mathrm{diag}(0.4, 0.43, 0.64),$$
$$\mathbf{A}_{D,0} = \mathrm{diag}(0.1966, 0.1966, 0.83) \text{ [m}^2]$$
$$\mathbf{C}_{D,i} = \mathrm{diag}(0.4, 0.40, 0.61),$$
$$\mathbf{A}_{D,i} = \mathrm{diag}(0.092778, 0.092778, 0.19635) \text{ [m}^2],$$
$$i = 1, .., 3$$

The torque due to wind, $^0\mathbf{n}_{w,0}$, is calculated by assuming that the disturbance force is applied at $0.03 \, ^0\mathbf{e}_3$ [m] and $^i\mathbf{n}_{w,i}$ is applied at $0.01 \, ^i\mathbf{e}_3$ [m], $i = 1, .., 3$.

5.1.5 Parametric Uncertainties

To demonstrate controller robustness, the simulation includes parameter errors:

$$\widehat{b}_T = b_T - 0.1b_T, \widehat{b}_m = b_m - 0.32b_m \tag{47a}$$
$$\widehat{m}_0 = m_0 - 0.1m_0, \widehat{m}_i = m_i + 0.034m_i, \widehat{^i\mathbf{J}_i} = {}^i\mathbf{J}_i + 0.33 \, ^i\mathbf{J}_i \tag{47b}$$

The capabilities of the UAV are tested via a precision flight maneuver, during which the UAV follows a desired pose trajectory; a maneuver where the UAV recovers from a large initial pose error is carried out also. The initial conditions (ICs) for all simulations are:

$$^I\mathbf{x}_0(0) = [0, 0, 0.0965]^T \text{ [m]}, {}^I\mathbf{v}_0(0)=\mathbf{0} \text{ [m/s]} \tag{48a}$$
$$^I\mathbf{R}_0(0) = \mathbf{1}, {}^0\boldsymbol{\omega}_0(0)=\mathbf{0} \text{ [rad/s]} \tag{48b}$$
$$^I\mathbf{R}_i(0) \approx \mathbf{1}, {}^i\boldsymbol{\omega}_i(0)=744.6001 \, ^i\mathbf{e}_3 \text{ [rad/s]}, i=1, .., 3 \tag{48c}$$

5.2 High Precision Surveillance Flight Maneuver

To demonstrate independent position-attitude regulation as well as the effectiveness and robustness of the control strategy, a complex figure "R" type trajectory is performed (generated using "minimum-snap" polynomials [37]), while at the same time a camera (fixed to the vehicle) is pointed at a target (KUKA youBot, see Fig. 6a). The series of way-points used for trajectory generation are given in the Appendix, Section A.6.

The results are shown in Fig. 6 and in the Supplementary video file (third flight scenario). Snapshots of the UAV's pose trajectory (via ROS-Gazebo) are visible in Fig. 6a; the trajectory is accurately tracked. The attitude response is shown in Fig. 6c; via Eq. (35), the percentage attitude error remains below $\Psi_0=1.5\%$ (see Fig. 6c, 3rd row) and the desired yaw/pitch orientation is smoothly tracked (see Fig. 6c, $1^{st}/2^{nd}$ row). The roll response is maintained close to zero (not shown due to space limitations). Except from a steady state altitude tracking error, $|e_{x_3}|<0.0975$ [m] (see Fig. 6b, 3rd row), the controller is robust. The soft allocation gains, see Table 1, are the cause. The control effort for

Fig. 6 UAV figure "R" tracking. (6a) UAV initial to final pose tracking response. (6b) Position response (Blue: state, Black: desired). (6c) Base attitude response via Euler angles, and percentage attitude, $\Psi_{0_\%}$. (6d) Control inputs, $^2\mathbf{u}_2$ Nm
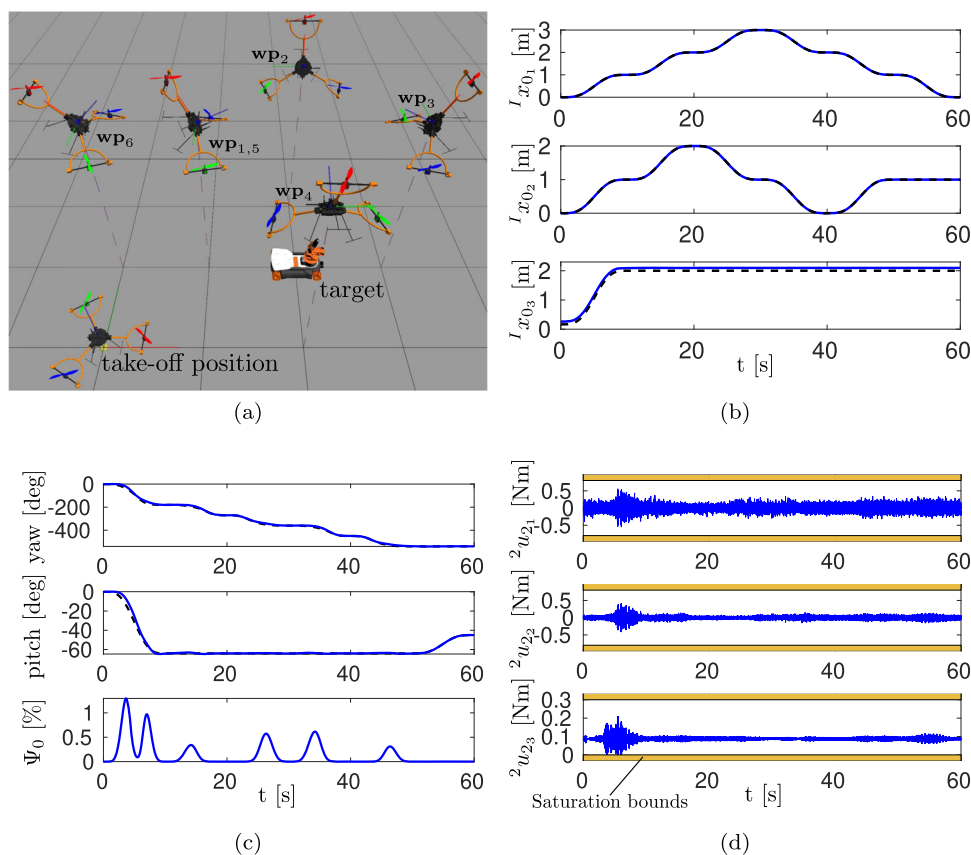
pointing and spinning the second TA is shown in Fig. 6d; saturation bounds are defined per Eq. (46). Due to the disturbances, actuator saturation is observed, see Fig. 6d. Via Eq. (23), the percentage pointing error is $\Psi_{2_\%} < 0.04\,\%$ (not shown due to space limitations). The response of the other TAs is omitted; they exhibit similar response.

5.3 Point to Point Motion

The next simulation shows the ability of the platform to perform motions of large initial pose error. A change from the ICs in Eq. (48), to:

$$^I\mathbf{x}_{0_d} = [0;\,0;\,1]\,[\text{m}],\ ^I\mathbf{v}_{0_d} = \mathbf{0}\,[\text{m/s}]$$

$$^I\mathbf{R}_0^{0_d} = \begin{bmatrix} 1 & 0 & 0 \\ 0 & 0.8660 & 0.5000 \\ 0 & -0.5000 & 0.8660 \end{bmatrix},\ ^0\boldsymbol{\omega}_{0_d} = \mathbf{0}\,[\text{rad/s}],\ ^0\dot{\boldsymbol{\omega}}_{0_d} = \mathbf{0}\,[\text{rad/s}^2]$$

is the goal; $^I\mathbf{R}_0^{0_d}$ expresses a 30° pitch maneuver about the $^0\mathbf{e}_1$ axis.

The performed step maneuver is shown in Fig. 7 and in the Supplementary video file (first flight scenario). A successful transition to the desired position, Fig. 7a (1st row), and attitude, Fig. 7a (2nd row), is shown; the dashed line in the 2nd row denotes the desired command. The response of the yaw and roll angles is omitted because they stay close to zero since a pitch only variation is conducted. A percentage pointing error, $\Psi_{i_\%} < 0.02\,\%$, is observed, see Fig. 7b; it is quickly driven to zero. The control input for the 1st-TA is shown in Fig. 7c; similar response is observed for the other TAs. To avoid actuator saturation, soft K_x, K_v, K_R, K_Ω gains were selected; saturation is observed only in the third row in Fig. 7c. The torque-speed response of the 1st-TA's pointing actuators is shown in Fig. 7d for the Dynamixel XL430-W250T actuator [35]; the response shows that the design is feasible using readily available actuators.

Concluding, the ability of the developed system/controller in achieving robustly independent position/attitude regulation, in the presence of parametric uncertainties, signal estimation errors, actuator saturation, measurement noise, and disturbances was demonstrated, both in a precision pose tracking setting and for a large step/error pose recovery maneuver.

Fig. 7 UAV point to point
recovery maneuver. (7a) Top:
Position error (norm). Middle:
Pitch attitude response (Blue:
state, Black: desired). Bottom:
Initial pose (left) vs. final pose
(right). (7b) Percentage attitude
error for each TA via Eq. (23).
(7c) 1st-TA control torque, $^1\mathbf{u}_1$.
(7d) Torque-speed response for
the 1st-TA. The characteristic
line is for the Dynamixel
XL430-W250T actuator [35]

(a)

(b)

(c)

(d)
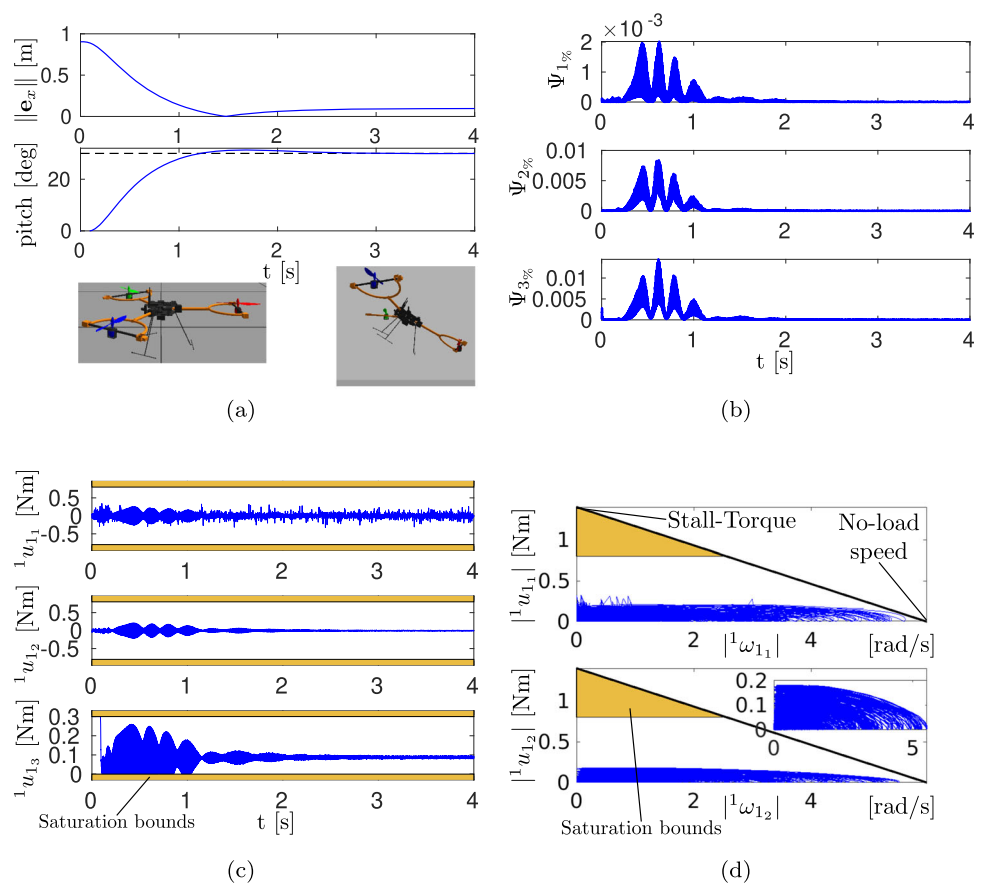
6 Conclusion

A novel design for a holonomic Unmanned Aerial Vehicle
(HUAV) using three vectored high-power thrusting actu-
ators (TAs) was developed. The pointing motion of high
rpm motor-propeller assemblies is accompanied by oscil-
latory gyroscopic dynamics. These dynamics were studied
analytically to yield vectoring oscillation frequency esti-
mates, useful in selecting actuators. Taking into account
the dynamics/high angular momentum of the high rpm
motor-propeller assemblies, a new vectoring controller able
to regulate the motion of the TAs was developed. A new
body-0 output tracking control law and allocation scheme
was developed yielding vectoring controller commands and
achieving full pose control. Stability proofs demonstrated,
vectoring controller stability under parametric uncertainties,
bounded signal estimation errors and bounded disturbances.
Overall system stability/robustness under bounded distur-
bances was demonstrated in the same manner. Simulations
(MATLAB and ROS/GAZEBO) illustrated the feasibility
of the developed design and control framework via three

different simulation scenarios; a HUAV with independent
position/attitude regulation (full pose control) was illus-
trated, naturally assuming any pose of interest.

Appendix A: Supplementary Material

A.1 Mappings & Kinematics used in Section 2.2

Cross product map, first used in Eq. (1)

$$S : \mathbb{R}^3 \to \mathfrak{so}(3), \text{ with}$$
$$S(\mathbf{r})=[0, -r_3, r_2; r_3, 0, -r_1; -r_2, r_1, 0], \ S^{-1}(S(\mathbf{r}))=\mathbf{r} \tag{A1}$$

where $\mathfrak{so}(3)$ is the set of all 3×3 skew symmetric matrices.

Velocity and acceleration of the CM of the ith-TA, first
used in Eq. (1)

$$^I\mathbf{v}_i = {}^I\mathbf{v}_0 + {}^I\dot{\mathbf{R}}_0{}^0\mathbf{r}_i - {}^I\dot{\mathbf{R}}_i{}^i\mathbf{p}_i \tag{A2a}$$
$$^I\dot{\mathbf{v}}_i = {}^I\dot{\mathbf{v}}_0 + {}^I\ddot{\mathbf{R}}_0{}^0\mathbf{r}_i - {}^I\ddot{\mathbf{R}}_i{}^i\mathbf{p}_i \tag{A2b}$$

A.2 Terms of Eq. (8) used in Section 2.2

Control input matrix, $\mathbf{B} \in \mathbb{R}^{15 \times 9}$, and mass matrix, $\mathbf{M} \in \mathbb{R}^{15 \times 15}$, from Eq. (8) given by

$$\mathbf{B} = \begin{bmatrix} \mathbf{0}_{3 \times 3} & \mathbf{0}_{3 \times 3} & \mathbf{0}_{3 \times 3} \\ -^0\mathbf{R}_1 & -^0\mathbf{R}_2 & -^0\mathbf{R}_3 \\ \mathbf{1}_{3 \times 3} & \mathbf{0}_{3 \times 3} & \mathbf{0}_{3 \times 3} \\ \mathbf{0}_{3 \times 3} & \mathbf{1}_{3 \times 3} & \mathbf{0}_{3 \times 3} \\ \mathbf{0}_{3 \times 3} & \mathbf{0}_{3 \times 3} & \mathbf{1}_{3 \times 3} \end{bmatrix}, \ \mathbf{M} = \begin{bmatrix} M_{1,1} & M_{1,2} & M_{1,3} & M_{1,4} & M_{1,5} \\ M_{2,1} & M_{2,2} & M_{2,3} & M_{2,4} & M_{2,5} \\ M_{3,1} & M_{3,2} & M_{3,3} & 0 & 0 \\ M_{4,1} & M_{4,2} & 0 & M_{4,4} & 0 \\ M_{5,1} & M_{5,2} & 0 & 0 & M_{5,5} \end{bmatrix} \quad \text{(A3)}$$

where $M_{i,j} \in \mathbb{R}^{3 \times 3}$ are given by

$$M_{1,1} = \sum_{i=0}^{3} m_i \mathbf{1}, \ M_{1,2} = -\sum_{i=1}^{3} m_i{}^I\mathbf{R}_0 S\left({}^0\mathbf{r}_i\right),$$

$$M_{1,i+2} = m_i{}^I\mathbf{R}_i S\left({}^i\mathbf{p}_i\right), i = 1 - 3 \quad \text{(A4a)}$$

$$M_{2,1} = \sum_{i=1}^{3} S\left({}^0\mathbf{r}_i\right) m_i{}^0\mathbf{R}_I,$$

$$M_{2,2} = {}^0\mathbf{J}_0 - \sum_{i=1}^{3} S\left({}^0\mathbf{r}_i\right) m_i S\left({}^0\mathbf{r}_i\right) \quad \text{(A4b)}$$

$$M_{2,i+2} = S\left({}^0\mathbf{r}_i\right){}^0\mathbf{R}_i m_i S\left({}^i\mathbf{p}_i\right),$$

$$M_{i+2,1} = -S\left({}^i\mathbf{p}_i\right) m_i{}^i\mathbf{R}_I, i = 1 - 3 \quad \text{(A4c)}$$

$$M_{i+2,2} = S\left({}^i\mathbf{p}_i\right) m_i{}^i\mathbf{R}_0 S\left({}^0\mathbf{r}_i\right),$$

$$M_{i+2,i+2} = {}^i\mathbf{J}_i - S\left({}^i\mathbf{p}_i\right) m_i S\left({}^i\mathbf{p}_i\right), i = 1 - 3 \quad \text{(A4d)}$$

The components of $\mathbf{\Gamma} = [\Gamma_1, \Gamma_2, \Gamma_3, \Gamma_4, \Gamma_5]^T \in \mathbb{R}^{15 \times 1}$ from Eq. (8) are given by

$$\Gamma_1 = -\sum_{i=1}^{3} m_i{}^I\mathbf{\Phi}_i,$$

$$\Gamma_2 = -\sum_{i=1}^{3} S\left({}^0\mathbf{r}_i\right){}^0\mathbf{R}_I m_i{}^I\mathbf{\Phi}_i - S\left({}^0\boldsymbol{\omega}_0\right){}^0\mathbf{J}_0{}^0\boldsymbol{\omega}_0 \quad \text{(A5a)}$$

$$\Gamma_{i+2} = S\left({}^i\mathbf{p}_i\right) m_i{}^i\mathbf{R}_I{}^I\mathbf{\Phi}_i - S\left({}^i\boldsymbol{\omega}_i\right){}^i\mathbf{J}_i{}^i\boldsymbol{\omega}_i, i = 1 - 3 \quad \text{(A5b)}$$

where ${}^I\mathbf{\Phi}_i \in \mathbb{R}^{3 \times 3}$ is given by

$${}^I\mathbf{\Phi}_i = {}^I\mathbf{R}_0 S\left({}^0\boldsymbol{\omega}_0\right) S\left({}^0\boldsymbol{\omega}_0\right){}^0\mathbf{r}_i - {}^I\mathbf{R}_i S\left({}^i\boldsymbol{\omega}_i\right) S\left({}^i\boldsymbol{\omega}_i\right){}^i\mathbf{p}_i \quad \text{(A6a)}$$

The components of $\mathbf{G} = [G_1, G_2, G_3, G_4, G_5]^T \in \mathbb{R}^{15 \times 1}$ from Eq. (8) are given by

$$G_1 = \sum_{i=0}^{3} {}^I\mathbf{g}_i, G_2 = \sum_{i=1}^{3} S\left({}^0\mathbf{r}_i\right){}^0\mathbf{R}_I{}^I\mathbf{g}_i,$$

$$G_{i+2} = -S\left({}^i\mathbf{p}_i\right){}^i\mathbf{R}_I{}^I\mathbf{g}_i, i = 1 - 3 \quad \text{(A7)}$$

The components of $\mathbf{P} = [P_1, P_2, P_3, P_4, P_5]^T \in \mathbb{R}^{15 \times 1}$ from Eq. (8) are given by

$$P_1 = \sum_{i=1}^{3} {}^I\mathbf{R}_i{}^i\mathbf{f}_{p,i}, P_2 = \sum_{i=1}^{3} S\left({}^0\mathbf{r}_i\right){}^0\mathbf{R}_i{}^i\mathbf{f}_{p,i},$$

$$P_{i+2} = {}^i\mathbf{n}_{p,i} - S\left({}^i\mathbf{p}_i\right){}^i\mathbf{f}_{p,i}, i = 1 - 3 \quad \text{(A8)}$$

The components of $\mathbf{D} = [D_1, D_2, D_3, D_4, D_5]^T \in \mathbb{R}^{15 \times 1}$ from Eq. (8) are given by

$$D_1 = \sum_{i=0}^{3} {}^I\mathbf{f}_{w,i}, D_2 = \sum_{i=1}^{3} S\left({}^0\mathbf{r}_i\right){}^0\mathbf{R}_I{}^I\mathbf{f}_{w,i} + {}^0\mathbf{n}_{w,0} \quad \text{(A9a)}$$

$$D_{i+2} = {}^i\mathbf{n}_{w,i} - S\left({}^i\mathbf{p}_i\right){}^i\mathbf{R}_I{}^I\mathbf{f}_{w,i}, i = 1 - 3 \quad \text{(A9b)}$$

A.3 Vectoring Controller Terms used in Section 4.1

Pointing dynamics terms, first used in Eq. (9)

$${}^i\boldsymbol{\mathcal{J}}_i = {}^i\mathbf{J}_i - m_i\left(S\left({}^i\mathbf{p}_i\right)\right)^2 \quad \text{(A10a)}$$

$${}^i\mathbf{Z}_i = S\left({}^i\mathbf{p}_i\right){}^i\mathbf{R}_I m_i{}^I\mathbf{\Xi}_i - {}^i\mathbf{J}_i{}^i\mathbf{R}_0 \quad \text{(A10b)}$$

$${}^I\mathbf{\Xi}_i = {}^I\mathbf{R}_i S\left({}^i\mathbf{p}_i\right){}^i\mathbf{R}_0 - {}^I\mathbf{R}_0 S\left({}^0\mathbf{r}_i\right) \quad \text{(A10c)}$$

$${}^i\mathbf{n}_{r,i} = {}^i\mathbf{J}_i S\left({}^i\boldsymbol{\omega}_{i/0}\right){}^i\mathbf{R}_0{}^0\boldsymbol{\omega}_0 - S\left({}^i\boldsymbol{\omega}_i\right){}^i\mathbf{J}_i{}^i\boldsymbol{\omega}_i$$
$$\quad + S\left({}^i\mathbf{p}_i\right){}^i\mathbf{R}_I\left(m_i\left({}^I\mathbf{k}_i - {}^I\mathbf{R}_i\left(S({}^i\boldsymbol{\omega}_{i/0})\right)^2{}^i\mathbf{p}_i\right) - {}^I\mathbf{g}_i\right)$$
$$\quad + \left(-\mathrm{sgn}\left({}^i\omega_{i_3}\right) b_m\mathbf{1} - S\left({}^i\mathbf{p}_i\right)\right){}^i\mathbf{f}_{p,i} \quad \text{(A10d)}$$

where the term ${}^I\mathbf{k}_i \in \mathbb{R}^{3 \times 1}$ used above and throughout the manuscript is given by

$${}^I\mathbf{k}_i = {}^I\mathbf{R}_0\left(S\left({}^0\boldsymbol{\omega}_0\right)\right)^2{}^0\mathbf{r}_i - {}^I\mathbf{R}_i S\left({}^i\mathbf{p}_i\right) S\left({}^i\boldsymbol{\omega}_{i/0}\right){}^i\mathbf{R}_0{}^0\boldsymbol{\omega}_0$$
$$\quad - {}^I\mathbf{R}_i\left(\left(S\left({}^i\mathbf{R}_0{}^0\boldsymbol{\omega}_0\right)\right)^2 + S\left({}^i\mathbf{R}_0{}^0\boldsymbol{\omega}_0\right) S\left({}^i\boldsymbol{\omega}_{i/0}\right)\right.$$
$$\quad \left. + S\left({}^i\boldsymbol{\omega}_{i/0}\right) S\left({}^i\mathbf{R}_0{}^0\boldsymbol{\omega}_0\right)\right){}^i\mathbf{p}_i \quad \text{(A11)}$$

A.4 Feedback terms used in Section 4.2

Attitude error function bounding inequality, [30], first used in Eq. (C4)

$$\|\mathbf{e}_R\|^2 \leq \Psi_0 \leq 2\|\mathbf{e}_R\|^2 \quad \text{(A12)}$$

Error function (attitude error vector) derivatives $\dot{\boldsymbol{\psi}}_0$ ($\dot{\mathbf{e}}_R$), [30], first used in Eq. (39)

$$\dot{\boldsymbol{\psi}}_0 = \mathbf{e}_R^T \mathbf{e}_\omega \tag{A13a}$$

$$\dot{\mathbf{e}}_R = {}^0\mathbf{E}\,\mathbf{e}_\omega \tag{A13b}$$

$${}^0\mathbf{E} = \frac{\left\{ \mathrm{tr}\left[{}^0\mathbf{R}_I{}^I\mathbf{R}_0^{0_d} \right] \mathbf{1} - {}^0\mathbf{R}_I{}^I\mathbf{R}_0^{0_d} + 2\mathbf{e}_R\mathbf{e}_R^T \right\}}{2\sqrt{1 + tr\left[{}^0\mathbf{R}_I{}^I\mathbf{R}_0^{0_d} \right]}} \tag{A13c}$$

Supporting term ${}^0\mathbf{a}_0 \in \mathbb{R}^{3\times1}$, first used in Eq. (39)

$${}^0\mathbf{a}_0 = S\left({}^0\boldsymbol{\omega}_0 \right){}^0\mathbf{R}_I{}^I\mathbf{R}_0^{0_d}\,{}^0\boldsymbol{\omega}_{0_d} - {}^0\mathbf{R}_I{}^I\mathbf{R}_0^{0_d}\,{}^0\dot{\boldsymbol{\omega}}_{0_d} \tag{A14}$$

Vectors $\mathbf{h}_p$, $\mathbf{h}_g \in \mathbb{R}^{6\times1}$, first used in used Eq. (37)

$$\mathbf{h}_p = b_T \sum_{i=1}^3 \left[{}^I\mathbf{R}_0{}^0\mathbf{h}_{p,i}; \mathbf{A}_i{}^I\mathbf{R}_0{}^0\mathbf{h}_{p,i} \right] \tag{A15a}$$

$$\begin{aligned}{}^0\mathbf{h}_{p,i} = &\,{}^0\mathbf{q}_i \left(2\left({}^i\mathbf{e}_3^{T\,i}\boldsymbol{\omega}_{i/0} \right)\left(\left({}^i\mathbf{R}_0{}^0\boldsymbol{\omega}_0 \right)^{T\,i}\mathbf{e}_3 \right) + \left(\left({}^i\mathbf{R}_0{}^0\boldsymbol{\omega}_0 \right)^{T\,i}\mathbf{e}_3 \right)^2 \right) \\ &- {}^0\mathbf{q}_{i_d} \left(2\left({}^i\mathbf{e}_3^{T\,i}\boldsymbol{\omega}_{i_d/0} \right)\left(\left({}^i\mathbf{R}_0^{i_d}{}^0\boldsymbol{\omega}_0 \right)^{T\,i}\mathbf{e}_3 \right) \right. \\ &\left. + \left(\left({}^i\mathbf{R}_0^{i_d}{}^0\boldsymbol{\omega}_0 \right)^{T\,i}\mathbf{e}_3 \right)^2 \right) \end{aligned} \tag{A15b}$$

$$\mathbf{h}_g = \left[{}^I\mathbf{h}_{g_1}; {}^0\mathbf{h}_{g_2} \right] \tag{A15c}$$

$${}^I\mathbf{h}_{g_1} = -{}^I\mathbf{g}_0 + \sum_{i=1}^3 \left(m_i{}^I\mathbf{k}_i - {}^I\mathbf{g}_i \right) \tag{A15d}$$

$$\begin{aligned}{}^0\mathbf{h}_{g_2} = &\,{}^0\boldsymbol{\omega}_0 \times {}^0\mathbf{J}_0{}^0\boldsymbol{\omega}_0 - \sum_{i=1}^3 {}^0\mathbf{R}_I{}^I\mathbf{R}_i{}^i\mathbf{J}_i S\left({}^i\boldsymbol{\omega}_{i/0} \right){}^i\mathbf{R}_0{}^0\boldsymbol{\omega}_0 \\ &- \sum_{i=1}^3 {}^0\boldsymbol{\Theta}_i{}^i\mathbf{R}_I\left(m_i{}^I\mathbf{k}_i - {}^I\mathbf{g}_i \right) + \sum_{i=1}^3 {}^0\mathbf{R}_I{}^I\mathbf{R}_i{}^i\mathbf{y}_i \end{aligned} \tag{A15e}$$

where the terms ${}^0\boldsymbol{\Theta}_i \in \mathbb{R}^{3\times3}$, ${}^i\mathbf{y}_i \in \mathbb{R}^{3\times1}$, $\mathbf{A}_i \in \mathbb{R}^{3\times3}$ used above and throughout the manuscript are given by

$${}^0\boldsymbol{\Theta}_i = {}^0\mathbf{R}_I{}^I\mathbf{R}_i S\left({}^i\mathbf{p}_i \right) - S\left({}^0\mathbf{r}_i \right){}^0\mathbf{R}_I{}^I\mathbf{R}_i \tag{A16a}$$

$$\begin{aligned}{}^i\mathbf{y}_i = &\, S\left({}^i\mathbf{R}_0{}^0\boldsymbol{\omega}_0 \right){}^i\mathbf{J}_i{}^i\mathbf{R}_0{}^0\boldsymbol{\omega}_0 + S\left({}^i\mathbf{R}_0{}^0\boldsymbol{\omega}_0 \right){}^i\mathbf{J}_i{}^i\boldsymbol{\omega}_{i/0} \\ &+ S\left({}^i\boldsymbol{\omega}_{i/0} \right){}^i\mathbf{J}_i{}^i\mathbf{R}_0{}^0\boldsymbol{\omega}_0 \end{aligned} \tag{A16b}$$

$$\mathbf{A}_i = -\mathrm{sgn}\left({}^i\omega_3 \right) b_m{}^0\mathbf{R}_I - {}^0\boldsymbol{\Theta}_i{}^i\mathbf{R}_I \tag{A16c}$$

and for ${}^I\mathbf{k}_i \in \mathbb{R}^{3\times1}$, see Eq. (A11).

Matrix term $\mathbf{C} \in \mathbb{R}^{6\times6}$, first used in Eq. (37)

$$\mathbf{C} = \begin{bmatrix} \left(m_0 + \sum_{i=1}^3 m_i \right)\mathbf{1} & \sum_{i=1}^3 m_i{}^I\boldsymbol{\Xi}_i \\ -\sum_{i=1}^3 {}^0\boldsymbol{\Theta}_i{}^i\mathbf{R}_I m_i & C_{2,2} \end{bmatrix} \tag{A17a}$$

$$C_{2,2} = {}^0\mathbf{J}_0 + \sum_{i=1}^3 \left({}^0\mathbf{R}_I{}^I\mathbf{R}_i{}^i\mathbf{J}_i{}^i\mathbf{R}_0 - {}^0\boldsymbol{\Theta}_i{}^i\mathbf{R}_I m_i{}^I\boldsymbol{\Xi}_i \right) \tag{A17b}$$

where ${}^I\boldsymbol{\Xi}_i$, ${}^0\boldsymbol{\Theta}_i \in \mathbb{R}^{3\times3}$ are given in Eqs. (A10c), (A16a).

Allocation matrix $\mathbf{A} \in \mathbb{R}^{6\times9}$, first used in Eq. 39

$$\mathbf{A} = [\mathbf{1}_{3\times3}, \mathbf{1}_{3\times3}, \mathbf{1}_{3\times3}; \mathbf{A}_1, \mathbf{A}_2, \mathbf{A}_3] \tag{A18}$$

and $\mathbf{A}_i \in \mathbb{R}^{3\times3}$ is given in Eq. (A16c).

A.5 Disturbance modeling term used in Section 5.1.2

Exponential map using the Rodrigues formulation [29], first used in Eq. (45)

$$\exp : \mathbb{R} \times \mathbb{R}^3 \to SO(3), \text{ with}$$
$$\exp(a, \boldsymbol{\xi}) = \mathbf{1} + S(\boldsymbol{\xi})\sin a + S(\boldsymbol{\xi})^2(1 - \cos a) \tag{A19}$$

A.6 Figure "R" pose trajectory used in Section 5.2

Way-points and pose continuity constraints used with minimum-snap polynomials for trajectory generation, employed in Section 5.2

$\mathbf{wp}_{0.0}|_{t=0}$: $\mathbf{x}_0 = [0, 0, 0.0965]^T$ [m], $\dot{\mathbf{x}}_0 = \mathbf{0}$ [m/s],
$\ddot{\mathbf{x}}_0 = \mathbf{0}$ [m/s^2], $\dddot{\mathbf{x}}_0 = \mathbf{0}$ [m/s^3]
$\mathbf{h} = [0, 0, 0]^T$ [deg], $\dot{\mathbf{h}} = \mathbf{0}$ [deg/s],
$\ddot{\mathbf{h}} = \mathbf{0}$ [deg/s^2], $\dddot{\mathbf{h}} = \mathbf{0}$ [deg/s^3]

$\mathbf{wp}_1|_{t=10}$: $\mathbf{x}_0 = [1, 1, 2]^T$ [m], $\dot{\mathbf{x}}_0 = \mathbf{0}$ [m/s],
$\ddot{\mathbf{x}}_0 = \mathbf{0}$ [m/s^2], $\dddot{\mathbf{x}}_0 = \mathbf{0}$ [m/s^3]
$\mathbf{h} = [-180, -64, 0]^T$ [deg], $\dot{\mathbf{h}} = \mathbf{0}$ [deg/s],
$\ddot{\mathbf{h}} = \mathbf{0}$ [deg/s^2], $\dddot{\mathbf{h}} = \mathbf{0}$ [deg/s^3]

$\mathbf{wp}_2|_{t=20}$: $\mathbf{x}_0 = [2, 2, 2]^T$ [m], $\dot{\mathbf{x}}_0 = \mathbf{0}$ [m/s], $\ddot{\mathbf{x}}_0 = \mathbf{0}$ [m/s^2],
$\dddot{\mathbf{x}}_0 = \mathbf{0}$ [m/s^3]
$\mathbf{h} = [-270, -64, 0]^T$ [deg], $\dot{\mathbf{h}} = \mathbf{0}$ [deg/s],
$\ddot{\mathbf{h}} = \mathbf{0}$ [deg/s^2], $\dddot{\mathbf{h}} = \mathbf{0}$ [deg/s^3]

$\mathbf{wp}_3|_{t=30}$: $\mathbf{x}_0 = [3, 1, 2]^T$ [m], $\dot{\mathbf{x}}_0 = \mathbf{0}$ [m/s], $\ddot{\mathbf{x}}_0 = \mathbf{0}$ [m/s^2],
$\dddot{\mathbf{x}}_0 = \mathbf{0}$ [m/s^3]
$\mathbf{h} = [-360, -64, 0]^T$ [deg], $\dot{\mathbf{h}} = \mathbf{0}$ [deg/s],
$\ddot{\mathbf{h}} = \mathbf{0}$ [deg/s^2], $\dddot{\mathbf{h}} = \mathbf{0}$ [deg/s^3]

$\mathbf{wp}_4|_{t=40}$: $\mathbf{x}_0 = [2, 0, 2]^T$ [m], $\dot{\mathbf{x}}_0 = \mathbf{0}$ [m/s], $\ddot{\mathbf{x}}_0 = \mathbf{0}$ [m/s^2],
$\dddot{\mathbf{x}}_0 = \mathbf{0}$ [m/s^3]
$\mathbf{h} = [-450, -64, 0]^T$ [deg], $\dot{\mathbf{h}} = \mathbf{0}$ [deg/s],
$\ddot{\mathbf{h}} = \mathbf{0}$ [deg/s^2], $\dddot{\mathbf{h}} = \mathbf{0}$ [deg/s^3]

$\mathbf{wp}_5|_{t=50}$: $\mathbf{x}_0 = [1, 1, 2]^T$ [m], $\dot{\mathbf{x}}_0 = \mathbf{0}$ [m/s], $\ddot{\mathbf{x}}_0 = \mathbf{0}$ [m/s^2],
$\dddot{\mathbf{x}}_0 = \mathbf{0}$ [m/s^3]
$\mathbf{h} = [-540, -64, 0]^T$ [deg], $\dot{\mathbf{h}} = \mathbf{0}$ [deg/s],
$\ddot{\mathbf{h}} = \mathbf{0}$ [deg/s^2], $\dddot{\mathbf{h}} = \mathbf{0}$ [deg/s^3]

$\mathbf{wp}_6|_{t=60}$: $\mathbf{x}_0 = [0, 1, 2]^T$ [m], $\dot{\mathbf{x}}_0 = \mathbf{0}$ [m/s], $\ddot{\mathbf{x}}_0 = \mathbf{0}$ [m/s^2],
$\dddot{\mathbf{x}}_0 = \mathbf{0}$ [m/s^3]
$\mathbf{h} = [-540, -45, 0]^T$ [deg], $\dot{\mathbf{h}} = \mathbf{0}$ [deg/s],
$\ddot{\mathbf{h}} = \mathbf{0}$ [deg/s^2], $\dddot{\mathbf{h}} = \mathbf{0}$ [deg/s^3]

where vector $\mathbf{h}$ components contain the desired yaw, pitch and roll commands.

Appendix B: Proof of Proposition 1

The following Lyapunov functions are defined

$$V_i\left(\Psi_i, {}^i\mathbf{e}_{q,i}, {}^i\mathbf{e}_{\omega,i}\right) = \frac{1}{2}{}^i\mathbf{s}_i^T\, {}^i\mathbf{s}_i + \alpha_i\Psi_i, \;\; i=1,2,3 \quad \text{(B1a)}$$

$$\alpha_i = 2\lambda_{\mathcal{J}_i}k_qk_\omega(\gamma_2+\gamma_3) \quad \text{(B1b)}$$

Note that Ψ_i and the error vectors appear explicitly in the Lyapunov function. Thus control design is similar to nonlinear control design in Euclidean spaces [38]. Via Eq. (25), it holds

$$\lambda_{min}(\boldsymbol{\Pi}_{1_i})\|\mathbf{z}_i\|^2 \le \mathbf{z}_i^T\boldsymbol{\Pi}_{1_i}\mathbf{z}_i \le V_i \le \mathbf{z}_i^T\boldsymbol{\Pi}_{2_i}\mathbf{z}_i \le \lambda_{max}(\boldsymbol{\Pi}_{2_i})\|\mathbf{z}_i\|^2$$
$$\text{(B2)}$$

where $\mathbf{z}_i = [\|{}^i\mathbf{e}_{q,i}\|; \|{}^i\mathbf{e}_{\omega,i}\|]$ and $\boldsymbol{\Pi}_{1_i}, \boldsymbol{\Pi}_{2_i} \in \mathbb{R}^{2\times2}$ are given by

$$\boldsymbol{\Pi}_{1_i} = \begin{bmatrix} \frac{(k_q+\Psi_i)^2+\alpha_i}{2} & -\frac{(k_q+\Psi_i)k_\omega}{2} \\ -\frac{(k_q+\Psi_i)k_\omega}{2} & k_\omega^2/2 \end{bmatrix}, \boldsymbol{\Pi}_{2_i} = \begin{bmatrix} \frac{(k_q+\Psi_i)^2}{2}+\frac{\alpha_i}{2-\Psi_i} & \frac{(k_q+\Psi_i)k_\omega}{2} \\ \frac{(k_q+\Psi_i)k_\omega}{2} & k_\omega^2/2 \end{bmatrix}$$
$$\text{(B3)}$$

The derivative of Eq. (28b) is needed to proceed. It is given by

$${}^i\dot{\mathbf{s}}_i = \dot{\Psi}_i\,{}^i\mathbf{e}_{q,i} + (k_q+\Psi_i)\,{}^i\dot{\mathbf{e}}_{q,i} + k_\omega\,{}^i\dot{\boldsymbol{\omega}}_{i/0} + k_\omega\,{}^i\mathbf{a}_i \quad \text{(B4)}$$

Differentiating Eq. (B1a) and using Eqs. (B4), (26a), (26c) results in

$$\dot{V}_i = {}^i\mathbf{s}_i^T\left(\dot{\Psi}_i\,{}^i\mathbf{e}_{q,i}+(k_q+\Psi_i)\,{}^i\dot{\mathbf{e}}_{q,i}+k_\omega\,{}^i\dot{\boldsymbol{\omega}}_{i/0}+k_\omega\,{}^i\mathbf{a}_i\right) + \alpha_i\dot{\Psi}_i$$
$$\text{(B5)}$$

Substituting into Eqs. (B5), (9), (28a), (26b), (27c), in the given order, after some manipulations

$$\dot{V}_i = {}^i\mathbf{s}_i^T\Big(\Delta\mathcal{J}_i\Big(\big({}^i\mathbf{e}_{q,i}\,{}^i\mathbf{e}_{q,i}^T\big)\,{}^i\mathbf{e}_{\omega,i}$$
$$+(k_q+\Psi_i)\,{}^i\mathcal{E}_i\,{}^i\mathbf{e}_{\boldsymbol{\omega},i}-k_\omega S\big({}^i\mathbf{R}_0{}^0\mathbf{R}_i^{i_d}\,{}^i\boldsymbol{\omega}_{i_d/0}\big)\,{}^i\mathbf{e}_{\boldsymbol{\omega},i}$$
$$-k_\omega\,{}^i\mathbf{R}_0{}^0\mathbf{R}_i^{i_d}\,{}^i\dot{\boldsymbol{\omega}}_{i_d/0}\big)-\gamma\,{}^i\mathcal{J}_i^{-1}\widehat{{}^i\mathcal{J}_i}\,{}^i\mathbf{s}_i$$
$$+k_\omega\,{}^i\mathcal{J}_i^{-1}\Big\{S\big({}^i\mathbf{p}_i\big)\,{}^i\mathbf{R}_I m_i\big({}^I\dot{\mathbf{v}}_0-{}^I\widehat{\dot{\mathbf{v}}_0}\big)$$
$$+\big({}^i\mathbf{Z}_i{}^0\dot{\boldsymbol{\omega}}_0-{}^i\widehat{\mathbf{Z}_i{}^0\dot{\boldsymbol{\omega}}_0}\big)+\big({}^i\mathbf{n}_{r,i}-{}^i\widehat{\mathbf{n}_{r,i}}\big)$$
$$+S\big({}^i\mathbf{p}_i\big)\,{}^i\mathbf{R}_I\big(-{}^I\mathbf{f}_{w,i}\big)+{}^i\mathbf{n}_{w,i}\Big\}\Big)+\alpha_i\,{}^i\mathbf{e}_{q,i}^T\,{}^i\mathbf{e}_{\omega,i} \quad \text{(B6a)}$$

$$\Delta\mathcal{J}_i = \mathbf{1}-{}^i\mathcal{J}_i^{-1}\widehat{{}^i\mathcal{J}_i} \quad \text{(B6b)}$$

After some rearranging, the above equation is given by

$$\dot{V}_i = {}^i\mathbf{s}_i^T\left({}^i\mathbf{N}_i{}^i\mathbf{e}_{\omega,i}+{}^i\mathbf{n}_{d,i}-\gamma\,{}^i\mathcal{J}_i^{-1}\widehat{{}^i\mathcal{J}_i}\,{}^i\mathbf{s}_i\right)+\alpha_i\,{}^i\mathbf{e}_{q,i}^T\,{}^i\mathbf{e}_{\omega,i} \quad \text{(B7a)}$$

$${}^i\mathbf{N}_i = {}^i\mathbf{N}_{n,i}-k_\omega\,{}^i\mathbf{N}_{\omega,i} \quad \text{(B7b)}$$

$${}^i\mathbf{n}_{d,i} = k_\omega\,{}^i\mathcal{J}_i^{-1}\Big\{S\big({}^i\mathbf{p}_i\big)\,{}^i\mathbf{R}_I m_i\big({}^I\dot{\mathbf{v}}_0-{}^I\widehat{\dot{\mathbf{v}}_0}\big)+\big({}^i\mathbf{Z}_i{}^0\dot{\boldsymbol{\omega}}_0-{}^i\widehat{\mathbf{Z}_i{}^0\dot{\boldsymbol{\omega}}_0}\big)$$
$$+\big({}^i\mathbf{n}_{r,i}-{}^i\widehat{\mathbf{n}_{r,i}}\big)+S\big({}^i\mathbf{p}_i\big)\,{}^i\mathbf{R}_I\big(-{}^I\mathbf{f}_{w,i}\big)+{}^i\mathbf{n}_{w,i}\Big\}$$
$$-\Delta\mathcal{J}_ik_\omega\,{}^i\mathbf{R}_0{}^0\mathbf{R}_i^{i_d}\,{}^i\dot{\boldsymbol{\omega}}_{i_d/0} \quad \text{(B7c)}$$

where ${}^i\mathbf{n}_{d,i}$ depends on the estimation errors, the disturbances and the desired angular acceleration and ${}^i\mathbf{N}_{n,i}, {}^i\mathbf{N}_{\omega,i}$, are given by

$${}^i\mathbf{N}_{n,i} = \Delta\mathcal{J}_i\left({}^i\mathbf{e}_{q,i}\,{}^i\mathbf{e}_{q,i}^T+(k_q+\Psi_i)\,{}^i\mathcal{E}_i\right) \quad \text{(B8a)}$$

$${}^i\mathbf{N}_{\omega,i} = \Delta\mathcal{J}_i S\left({}^i\mathbf{R}_0{}^0\mathbf{R}_i^{i_d}\,{}^i\boldsymbol{\omega}_{i_d/0}\right) \quad \text{(B8b)}$$

Inspecting the term ${}^i\mathcal{E}_i$ given in Eq. (27a), the magnitude of Eq. (B8) above depends on the desired trajectory. Additionally Eqs. (7), (32), (30a), (30b) imply that

$$\exists N_{n,i_{max}}, N_{\omega,i_{max}}, n_{d,i_{max}} \in (0,\infty)\big|\|{}^i\mathbf{N}_{n,i}\| \le N_{n,i_{max}}$$
$$\|{}^i\mathbf{N}_{\omega,i}\| \le N_{\omega,i_{max}}$$
$$\|{}^i\mathbf{n}_{d,i}\| \le n_{d,i_{max}} \quad \text{(B9)}$$

Employing Eq. (B9), the Lyapunov derivative in Eq. (B7a) is expanded to

$$\dot{V}_i \le -\gamma\lambda_{\mathcal{J}_i}\,{}^i\mathbf{s}_i^T\,{}^i\mathbf{s}_i + \Upsilon_i + \mathcal{N}_i\|{}^i\mathbf{e}_{\omega,i}\|$$
$$+\left(k_\omega N_{n,i_{max}}+k_\omega^2 N_{\omega,i_{max}}\right)\|{}^i\mathbf{e}_{\omega,i}\|^2+\alpha_i\,{}^i\mathbf{e}_{q,i}^T\,{}^i\mathbf{e}_{\omega,i} \quad \text{(B10a)}$$

$$\Upsilon_i = (k_q+\Psi_i)n_{d,i_{max}} \quad \text{(B10b)}$$

$$\mathcal{N}_i = k_\omega n_{d,i_{max}}+(k_q+\Psi_i)\left(N_{n,i_{max}}+k_\omega N_{\omega,i_{max}}\right) \quad \text{(B10c)}$$

Employing Eq. (28c) and rearranging

$$\dot{V}_i \le -\gamma_1\lambda_{\mathcal{J}_i}\,{}^i\mathbf{s}_i^T\,{}^i\mathbf{s}_i - \mathbf{z}_i^T\boldsymbol{\Pi}_{3_i}\mathbf{z}_i - \gamma_3\lambda_{\mathcal{J}_i}\,{}^i\mathbf{s}_i^T\,{}^i\mathbf{s}_i + \Upsilon_i + \mathcal{N}_i\|{}^i\mathbf{e}_{\omega,i}\|$$
$$+\left(k_\omega N_{n,i_{max}}+k_\omega^2 N_{\omega,i_{max}}\right)\|{}^i\mathbf{e}_{\omega,i}\|^2+2\lambda_{\mathcal{J}_i}k_qk_\omega\gamma_3\,{}^i\mathbf{e}_{q,i}^T\,{}^i\mathbf{e}_{\omega,i} \quad \text{(B11a)}$$

$$\boldsymbol{\Pi}_{3_i} = \begin{bmatrix} \gamma_2\lambda_{\mathcal{J}_i}(k_q+\Psi_i)^2 & -\gamma_2\lambda_{\mathcal{J}_i}\Psi_ik_\omega \\ -\gamma_2\lambda_{\mathcal{J}_i}\Psi_ik_\omega & \gamma_2\lambda_{\mathcal{J}_i}k_\omega^2 \end{bmatrix} \quad \text{(B11b)}$$

Via $\gamma_3 = \sum_{i=4}^5\gamma_i, \gamma_i, \in \mathbb{R}^+$ after some manipulations

$$\dot{V}_i \le -\gamma_1\lambda_{\mathcal{J}_i}\,{}^i\mathbf{s}_i^T\,{}^i\mathbf{s}_i - \mathbf{z}_i^T\boldsymbol{\Pi}_{3_i}\mathbf{z}_i$$
$$-\mathbf{z}_i^T\boldsymbol{\Pi}_{4_i}\mathbf{z}_i + \Upsilon_i + \phi\left(\|{}^i\mathbf{e}_{\omega,i}\|\right) \quad \text{(B12a)}$$

$$\phi\left(\|{}^i\mathbf{e}_{\omega,i}\|\right) = \mathcal{N}_i\|{}^i\mathbf{e}_{\omega,i}\|$$
$$-\left((\gamma_5\lambda_{\mathcal{J}_i}-N_{\omega,i_{max}})k_\omega^2-k_\omega N_{n,i_{max}}\right)\|{}^i\mathbf{e}_{\omega,i}\|^2 \quad \text{(B12b)}$$

$$\boldsymbol{\Pi}_{4_i} = \begin{bmatrix} \gamma_3\lambda_{\mathcal{J}_i}(k_q+\Psi_i)^2 & -\gamma_3\lambda_{\mathcal{J}_i}\Psi_ik_\omega \\ -\gamma_3\lambda_{\mathcal{J}_i}\Psi_ik_\omega & \gamma_4\lambda_{\mathcal{J}_i}k_\omega^2 \end{bmatrix} \quad \text{(B12c)}$$

The condition in Eq. (28f) ensures that matrix $\boldsymbol{\Pi}_{4_i}$ is positive definite. Conditions in Eqs. (28d), (28e), ensure that the last term of Eq. (B12b) is non-positive. For an angular velocity error vector, $^i\mathbf{e}_{\omega,i}$, such that

$$\|^i\mathbf{e}_{\omega,i}\| > \frac{\mathcal{N}_i}{\left(\gamma_5\lambda_{\mathcal{J}_i}-N_{\omega,i_{max}}\right)k_\omega^2 - k_\omega N_{n,i_{max}}} \quad (B13)$$

then Eq. (B12b) is non-positive. Additionally for $\|^i\mathbf{e}_{\omega,i}\|$ less or equal to Eqs. (B13), (B12b) is bounded by

$$\phi\left(\|^i\mathbf{e}_{\omega,i}\|\right) \leq \frac{\mathcal{N}_i^2}{4\left(\gamma_5\lambda_{\mathcal{J}_i}-N_{\omega,i_{max}}\right)k_\omega^2 - 4k_\omega N_{n,i_{max}}}, \forall t \quad (B14)$$

Thus the following inequality is valid

$$\dot{V}_i \leq -\gamma_1\lambda_{\mathcal{J}_i}{}^i\mathbf{s}_i^{T\,i}\mathbf{s}_i - \lambda_{min}(\boldsymbol{\Pi}_{3_i})\|\mathbf{z}_i\|^2 - \lambda_{min}(\boldsymbol{\Pi}_{4_i})\|\mathbf{z}_i\|^2 + \delta_i \quad (B15a)$$

$$\delta_i = \Upsilon_i + \frac{\mathcal{N}_i^2}{4(\gamma_5\lambda_{\mathcal{J}_i}-N_{\omega,i_{max}})k_\omega^2 - 4k_\omega N_{n,i_{max}}} \quad (B15b)$$

Concluding, for $\mathbf{z}_i$ such that

$$\|\mathbf{z}_i\| \geq \sqrt{\frac{\delta_i}{\lambda_{min}(\boldsymbol{\Pi}_{3_i})}} \quad (B16)$$

then

$$\dot{V}_i \leq -\gamma_1\lambda_{\mathcal{J}_i}{}^i\mathbf{s}_i^{T\,i}\mathbf{s}_i - \lambda_{min}(\boldsymbol{\Pi}_{4_i})\|\mathbf{z}_i\|^2 \leq -\lambda_{min}(\boldsymbol{\Pi}_{4_i})\|\mathbf{z}_i\|^2 \quad (B17)$$

The first term in Eq. (B17) ensures the desired sliding behavior. Finally using Eq. (B2)

$$\dot{V}_i \leq -(\lambda_{min}(\boldsymbol{\Pi}_{4_i})/\lambda_{max}(\boldsymbol{\Pi}_{2_i}))V_i \quad (B18)$$

Boundedness: Using Eq. (B16), the following sets are defined

$$\mathrm{L}_\sigma = \left\{\left(^i\mathbf{e}_{q,i}, {}^i\mathbf{e}_{\omega,i}\right) \in \mathbb{R}^3\times\mathbb{R}^3 \mid \text{Eq. (B16)}\right\} \quad (B19a)$$

$$\mathrm{L}_\phi = \left\{\left(^i\mathbf{e}_{q,i}, {}^i\mathbf{e}_{\omega,i}\right) \in \mathbb{R}^3\times\mathbb{R}^3 \mid \Psi_i < 2\right\} \quad (B19b)$$

For a gain γ such that, Eq. (33) is satisfied, then $\mathrm{L}_\sigma^c \subset \mathrm{L}_\phi$ $((.)^c$ is the complement set of $(.))$. Hence, Eq. (B18) implies that for all initial states beginning in L_ϕ, it holds that

$$\alpha_i\Psi_i \leq V_i(t) \leq V_i(0)e^{-\frac{\lambda_{min}(\boldsymbol{\Pi}_{4_i})}{\lambda_{max}(\boldsymbol{\Pi}_{2_i})}t} \quad (B20)$$

Thus Ψ_i exponentially decreases and the pointing tracking errors exponentially converge to L_σ^c and are UUB despite the presence of parametric uncertainties, disturbances and signal estimation errors. An estimate of the ultimate bound is given in Eq. (34).

Inspecting Eqs. (B15b), (B11b), if γ_2 is increased, $\lambda_{min}(\boldsymbol{\Pi}_{3_i})$ increases also. Since both Eqs. (B10b), (B10c) (they comprise δ_i), are a function of the estimation errors,

the disturbances and the attitude errors which are all bounded, for suitable γ_2, γ_5 (γ_5 reduces Eq. (B15b)) the conditions of Eq. (33) are satisfied. However depending on the actuator/thrust constraints the value of γ_2, γ_5 is limited. In this case Eq. (33) is satisfied for less aggressive trajectories, smaller estimation errors and smaller disturbances.

Appendix C: Proof of Proposition 2

C.1 Body-0 Attitude Error Dynamics

First the derivative of Eq. (36b) is calculated. Then Eqs. (6b), (6c), are substituted in the derivative followed by Eqs. (1c), (3). Finally Eqs. (A2b) and (5), are substituted into the resulting expression to get

$$\dot{\mathbf{e}}_{\mathbf{v},\boldsymbol{\omega}} = \mathbf{C}^{-1}\left(\sum_{i=1}^{3}\begin{bmatrix}{}^I\mathbf{R}_i{}^i\mathbf{f}_{p,i}\\ \mathbf{A}_i{}^I\mathbf{R}_i{}^i\mathbf{f}_{p,i}\end{bmatrix} - \mathbf{d} - \mathbf{h}_g\right) + \begin{bmatrix}-{}^I\dot{\mathbf{v}}_d\\ {}^0\mathbf{a}_0\end{bmatrix} \quad (C1)$$

where $\mathbf{A}_i \in \mathbb{R}^{3\times3}$ is given in Eq. (A16c). The vector $\mathbf{d} = [d_1; d_2] \in \mathbb{R}^{6\times1}$ is given by

$$d_1 = \sum_{i=1}^{3}\left(m_i{}^I\mathbf{R}_i S\left(^i\mathbf{p}_i\right){}^i\dot{\boldsymbol{\omega}}_{i/0} - {}^I\mathbf{f}_{w,i}\right.$$
$$\left. - m_i{}^I\mathbf{R}_i\left(S\left(^i\boldsymbol{\omega}_{i/0}\right)\right)^2{}^i\mathbf{p}_i\right) - {}^I\mathbf{f}_{w,0} \quad (C2a)$$

$$d_2 = \sum_{i=1}^{3}{}^0\mathbf{R}_I{}^I\mathbf{R}_i\left\{^i\mathbf{J}_i{}^i\dot{\boldsymbol{\omega}}_{i/0} + S\left(^i\boldsymbol{\omega}_{i/0}\right){}^i\mathbf{J}_i{}^i\boldsymbol{\omega}_{i/0} - {}^i\mathbf{n}_{w,i}\right\} - {}^0\mathbf{n}_{w,0}$$
$$- \sum_{i=1}^{3}{}^0\boldsymbol{\Theta}_i{}^i\mathbf{R}_I\left(m_i{}^I\mathbf{R}_i S\left(^i\mathbf{p}_i\right){}^i\dot{\boldsymbol{\omega}}_{i/0} - {}^I\mathbf{f}_{w,i}\right.$$
$$\left. - m_i{}^I\mathbf{R}_i\left(S\left(^i\boldsymbol{\omega}_{i/0}\right)\right)^2{}^i\mathbf{p}_i\right) \quad (C2b)$$

where the matrix ${}^0\boldsymbol{\Theta}_i \in \mathbb{R}^{3\times3}$ is given in Eq. (A16a). Vector $\mathbf{d}$ contains bounded disturbance terms (see Eq. (7)); under the action of Eq. (28a), the relative angular velocity and acceleration terms, $^i\boldsymbol{\omega}_{i/0}, {}^i\dot{\boldsymbol{\omega}}_{i/0}$, of each TA with respect to body-0 are stable and bounded (see proof of Proposition 1 or/and see Section 4.4.1). Thus vector $\mathbf{d}$ is bounded and small; the small mass-inertia characteristics and geometry of each TA contributes to this also.

C.2 Lyapunov Analysis

For $\zeta_1, \zeta_2 \in \mathbb{R}^+$ such that Eq. (37b) is satisfied, the following Lyapunov function is defined

$$V = \frac{1}{2}\mathbf{z}^T\mathbf{z} + \zeta_1 K_x K_v \mathbf{e}_x^T\mathbf{e}_x + 2\zeta_1 K_\Omega K_R\Psi_0 \quad (C3)$$

Defining $\mathbf{z}_c = [\|\mathbf{e}_x\|; \|\mathbf{e}_v\|; \|\mathbf{e}_R\|; \|\mathbf{e}_\omega\|] \in \mathbb{R}^4$ and via Eq. (A12) the Lyapunov function is bounded by

$$\lambda_{min}(\mathcal{W}_1)\|\mathbf{z}_c\|^2 \leq \mathbf{z}_c^T\mathcal{W}_1\mathbf{z}_c \leq V \leq \mathbf{z}_c^T\mathcal{W}_2\mathbf{z}_c \leq \lambda_{max}(\mathcal{W}_2)\|\mathbf{z}_c\|^2 \quad \text{(C4a)}$$

$$\mathcal{W}_1 = \begin{bmatrix} \frac{K_x^2}{2}+\zeta_1 K_x K_v & -\frac{K_x K_v}{2} & 0 & 0 \\ -\frac{K_x K_v}{2} & \frac{K_v^2}{2} & 0 & 0 \\ 0 & 0 & \frac{(K_R+\Psi_0)^2}{2}+2\zeta_1 K_\Omega K_R & -\frac{(K_R+\Psi_0)K_\Omega}{2} \\ 0 & 0 & -\frac{(K_R+\Psi_0)K_\Omega}{2} & \frac{K_\Omega^2}{2} \end{bmatrix} \quad \text{(C4b)}$$

$$\mathcal{W}_2 = \begin{bmatrix} \frac{K_x^2}{2}+\zeta_1 K_x K_v & \frac{K_x K_v}{2} & 0 & 0 \\ \frac{K_x K_v}{2} & \frac{K_v^2}{2} & 0 & 0 \\ 0 & 0 & \frac{(K_R+\Psi_0)^2}{2}+4\zeta_1 K_\Omega K_R & \frac{(K_R+\Psi_0)K_\Omega}{2} \\ 0 & 0 & \frac{(K_R+\Psi_0)K_\Omega}{2} & \frac{K_\Omega^2}{2} \end{bmatrix} \quad \text{(C4c)}$$

The time derivative of the Lyapunov function is given by,

$$\dot{V} = \mathbf{z}^T\left(\begin{bmatrix} K_v\mathbf{1} & 0_{3\times3} \\ 0_{3\times3} & K_\Omega\mathbf{1} \end{bmatrix}\dot{\mathbf{e}}_{\mathbf{v},\omega} + \begin{bmatrix} K_x\mathbf{e}_v \\ (K_R+\Psi_0)\dot{\mathbf{e}}_R+\dot{\Psi}_0\mathbf{e}_R \end{bmatrix}\right)$$
$$+2\zeta_1 K_x K_v \mathbf{e}_x^T\mathbf{e}_v + 2\zeta_1 K_\Omega K_R \mathbf{e}_R^T\mathbf{e}_\omega \quad \text{(C5)}$$

The thrust tracking error of each TA in $\mathscr{I}_0$, is given by the following algebraic relation

$${}^0\mathbf{R}_I\left({}^I\mathbf{R}_i{}^i\mathbf{f}_{p,i} - {}^I\mathbf{R}_i^{i_d}{}^{i_d}\mathbf{f}_{p,i_d}\right) = b_T{}^0\mathbf{q}_i\left({}^i\omega_i^{T\,i}\mathbf{e}_3\right)^2 - b_T{}^0\mathbf{q}_{i_d}\left({}^i\omega_{i_d}^{T\,i}\mathbf{e}_3\right)^2 \quad \text{(C6)}$$

Using Eq. (C6) together with Eqs. (20c), (22c) the ith TA generated thrust can be expressed by the following algebraic relation

$${}^I\mathbf{R}_i{}^i\mathbf{f}_{p,i} = {}^I\mathbf{R}_0\left({}^0\mathbf{f}_{p,i_e} + b_T{}^0\mathbf{h}_{p,i}\right) + {}^I\mathbf{R}_i^{i_d}{}^i\mathbf{f}_{p,i_d} \quad \text{(C7)}$$

where ${}^0\mathbf{h}_{p,i} \in \mathbb{R}^3$ is found in Eq. (A15b) and ${}^0\mathbf{f}_{p,i_e}$ is the thrust tracking error of each TA relative to body-0. It is given by

$${}^0\mathbf{f}_{p,i_e} = b_T{}^0\mathbf{q}_i\left({}^i\omega_{i/0}^{T\,i}\mathbf{e}_3\right)^2 - b_T{}^0\mathbf{q}_{i_d}\left({}^i\omega_{i_d/0}^{T\,i}\mathbf{e}_3\right)^2 \quad \text{(C8)}$$

Due to the action of the vectoring controller, ${}^0\mathbf{f}_{p,i_e}$ is small and bounded; because ${}^i\omega_{i/0}$ is bounded (see proof of Proposition 1 or/and see Section 4.4.1). Substituting Eqs. (C1) into (C5) followed by Eq. (C7), results in

$$\dot{V} = \mathbf{z}^T\left\{\begin{bmatrix} K_v\mathbf{1} & 0_{3\times3} \\ 0_{3\times3} & K_\Omega\mathbf{1} \end{bmatrix}\mathbf{C}^{-1}\left(\sum_{i=1}^{3}\left(\begin{bmatrix} {}^I\mathbf{R}_i^{i_d}{}^i\mathbf{f}_{p,i_d} \\ \mathbf{A}_i{}^I\mathbf{R}_i^{i_d}{}^i\mathbf{f}_{p,i_d} \end{bmatrix}\right.\right.\right.$$
$$\left.+ \begin{bmatrix} {}^I\mathbf{R}_0{}^0\mathbf{f}_{p,i_e} \\ \mathbf{A}_i{}^I\mathbf{R}_0{}^0\mathbf{f}_{p,i_e} \end{bmatrix}\right)-\mathbf{d}-\mathbf{h}_g+\mathbf{h}_p\right)$$
$$\left.+ \begin{bmatrix} -K_v\dot{\mathbf{v}}_d+K_x\mathbf{e}_v \\ K_\Omega{}^0\mathbf{a}_0+(K_R+\Psi_0)\dot{\mathbf{e}}_R+\dot{\Psi}_0\mathbf{e}_R \end{bmatrix}\right\}$$
$$+2\zeta_1 K_x K_v \mathbf{e}_x^T\mathbf{e}_v + 2\zeta_1 K_\Omega K_R \mathbf{e}_R^T\mathbf{e}_\omega \quad \text{(C9)}$$

By substituting Eqs. (39) in (C9), followed by Eq. (37), after considerable manipulations

$$\dot{V} = -\zeta\mathbf{z}^T\mathbf{z} + \mathbf{z}^T\boldsymbol{\epsilon}+2\zeta_1 K_x K_v\mathbf{e}_x^T\mathbf{e}_v + 2\zeta_1 K_\Omega K_R\mathbf{e}_R^T\mathbf{e}_\omega \quad \text{(C10a)}$$

$$\boldsymbol{\epsilon} = \begin{bmatrix} K_v\mathbf{1} & 0_{3\times3} \\ 0_{3\times3} & K_\Omega\mathbf{1} \end{bmatrix}\mathbf{C}^{-1}\left(\sum_{i=1}^{3}\begin{bmatrix} {}^I\mathbf{R}_0{}^0\mathbf{f}_{p,i_e} \\ \mathbf{A}_i{}^I\mathbf{R}_0{}^0\mathbf{f}_{p,i_e} \end{bmatrix}-\mathbf{d}\right) \quad \text{(C10b)}$$

$$\|\boldsymbol{\epsilon}\| \leq \epsilon_{max} \quad \text{(C10c)}$$

Note that vector $\boldsymbol{\epsilon}$ contains bounded quantities like disturbance terms. Due to space limitations the bound, ϵ_{max}, is not given explicitly but a conservative estimate can be found using Eqs. (7), (B16) and $\|{}^i\mathbf{e}_{q,i}\| \leq 1$. Employing that $\zeta = \zeta_1 + \zeta_2$, Eq. (C10a) is rearranged to

$$\dot{V}=-\zeta_1\mathbf{z}^T\mathbf{z}-\zeta_2\mathbf{z}^T\mathbf{z}+\mathbf{z}^T\boldsymbol{\epsilon}+2\zeta_1 K_x K_v\mathbf{e}_x^T\mathbf{e}_v+2\zeta_1 K_\Omega K_R\mathbf{e}_R^T\mathbf{e}_\omega \quad \text{(C11)}$$

Expanding the first term, after several manipulations

$$\dot{V} \leq -\mathbf{z}_c^T\mathcal{W}_3\mathbf{z}_c - \zeta_2\mathbf{z}^T\mathbf{z} + \mathbf{z}^T\boldsymbol{\epsilon} \quad \text{(C12a)}$$

$$\mathcal{W}_3 = \begin{bmatrix} \zeta_1 K_x^2 & 0 & 0 & 0 \\ 0 & \zeta_1 K_v^2 & 0 & 0 \\ 0 & 0 & \zeta_1(K_R+\Psi_0)^2 & -\zeta_1 K_\Omega\Psi_0 \\ 0 & 0 & -\zeta_1 K_\Omega\Psi_0 & \zeta_1 K_\Omega^2 \end{bmatrix} \quad \text{(C12b)}$$

Using the Cauchy-Schwarz inequality on Eq. (C12a)

$$\dot{V} \leq -\lambda_{min}(\mathcal{W}_3)\|\mathbf{z}_c\|^2 - \zeta_2\|\mathbf{z}\|^2 + \|\mathbf{z}\|\epsilon_{max} \implies$$
$$\forall\|\mathbf{z}\| \geq \frac{\epsilon_{max}}{\zeta_2} \implies \dot{V} < -\lambda_{min}(\mathcal{W}_3)\|\mathbf{z}_c\|^2 \quad \text{(C13)}$$

Furthermore via Eq. (C4a) the following holds

$$\dot{V} \leq -\frac{\lambda_{min}(\mathcal{W}_3)}{\lambda_{max}(\mathcal{W}_2)}V \quad \text{(C14)}$$

Concluding, via the comparison lemma, $\|\mathbf{z}_c\|$ exponentially decreases with a rate $e^{-\frac{\lambda_{min}(\mathcal{W}_3)}{\lambda_{max}(\mathcal{W}_2)}t}$ into an envelope of radius $\frac{\epsilon_{max}}{\zeta_2}$ of the origin and it is maintained there.

Boundedness: Based on the analysis above the following sets are defined,

$$\mathrm{L}_\varsigma = \left\{(\mathbf{e}_{\mathbf{x},R}, \mathbf{e}_{\mathbf{v},\omega}) \in \mathbb{R}^6\times\mathbb{R}^6 \mid \|\mathbf{z}\| \geq \frac{\epsilon_{max}}{\zeta_2}\right\} \quad \text{(C15a)}$$

$$\mathrm{L}_\Sigma = \left\{(\mathbf{e}_{\mathbf{x},R}, \mathbf{e}_{\mathbf{v},\omega}) \in \mathbb{R}^6\times\mathbb{R}^6 \mid \|\mathbf{z}\| < \sqrt{2\lambda_{max}(\mathcal{W}_2)}\right\} \quad \text{(C15b)}$$

For a sufficiently large gain ζ such that Eq. (43) is satisfied then $\mathrm{L}_\varsigma^c \subset \mathrm{L}_\Sigma$ $((.)^c$ the complement set of $(.)$). Hence, for all initial system states in L_Σ, the tracking errors ($\mathbf{e}_x$, $\mathbf{e}_v$, $\mathbf{e}_R$, $\mathbf{e}_\omega$) exponentially converge to L_ς^c and are UUB despite the presence of disturbances and thrust tracking errors. The boundary of the set L_ς^c is an estimate of the ultimate bound. Also Eqs. (C13), (C14), and (C15) indicate that as ζ is

increased, the error states converge faster to the desired equilibrium, while the ultimate bound set L_ς^c shrinks.

Code or data availability The authors attest that all data for this study are included in the paper.

Declarations

Ethics approval Not applicable.

Consent to participate Not applicable.

Consent for Publication Not applicable.

Conflict of Interests The authors declare that they have no conflict of interest.

References

1. Czyba, R., Szafranski, G., Rys, A.: Design and control of a single tilt tri-rotor aerial vehicle. J. Intell. Robot. Syst. **84**(1), 53–66 (2016). https://doi.org/10.1007/s10846-016-0353-0

2. Papachristos, C., Alexis, K., Tzes, A.: Dual-authority thrust-vectoring of a tri-tiltrotor employing model predictive control. J. Intell. Robot. Syst. **81**(3), 471–504 (2016). https://doi.org/10.1007/s10846-015-0231-1

3. Efraim, H., Shapiro, A., Weiss, G.: Quadrotor with a dihedral angle: on the effects of tilting the rotors inwards. J. Intell. Robot. Syst. **80**(2), 313–324 (2015). https://doi.org/10.1007/s10846-015-0176-4

4. Kanellakis, C., Nikolakopoulos, G.: Guidance for autonomous aerial manipulator using stereo vision. J. Intell. Robot. Syst. https://doi.org/10.1007/s10846-019-01060-8 (2019)

5. Loianno, G., Cross, G., Qu, C., Mulgaonkar, Y., Hesch, J.A., Kumar, V.: Flying smartphones: Automated flight enabled by consumer electronics. IEEE Robot. Autom. Mag. **22**(2), 24–32 (2015). https://doi.org/10.1109/MRA.2014.2382792

6. Nandakumar, G., Srinivasan, A., Thondiyath, A.: Theoretical and experimental investigations on the effect of overlap and offset on the design of a novel quadrotor configuration, voops. J. Intell. Robot. Syst. **92**(3), 615–628 (2018). https://doi.org/10.1007/s10846-017-0707-2

7. Guo, M., Gu, D., Zha, W., Zhu, X., Su, Y.: Controlling a quadrotor carrying a cable-suspended load to pass through a window. J.

8. Intell. Robot. Syst. **98**(2), 387–401 (2020). https://doi.org/10.1007/s10846-019-01038-6

8. Ryll, M., Bulthoff, H.H., Giordano, P.R.: Modeling and control of a quadrotor uav with tilting propellers. In: 2012 IEEE International Conference on Robotics and Automation, pp. 4606–4613, Saint Paul, MN, USA (2012). https://doi.org/10.1109/ICRA.2012.6225129

9. Ryll, M., Bulthoff, H.H., Giordano, P.R.: A novel overactuated quadrotor unmanned aerial vehicle: Modeling, control, and experimental validation. IEEE Trans. Control Syst. Technol. **23**(2), 540–556 (2015). https://doi.org/10.1109/TCST.2014.2330999

10. Segui-Gasco, P., Al-Rihani, Y., Shin, H.S., Savvaris, A.: A novel actuation concept for a multi rotor uav. J. Intell. Robot. Syst. **74**(1), 173–191 (2014). https://doi.org/10.1007/s10846-013-9987-3

11. Jiang, G., Voyles, R.: Hexrotor uav platform enabling dextrous interaction with structures-flight test. In: 2013 IEEE International Symposium on Safety, Security, and Rescue Robotics (SSRR), pp. 1–6, Linkoping, Sweden (2013). https://doi.org/10.1109/SSRR.2013.6719377

12. Jiang, G., Voyles, R.: A nonparallel hexrotor uav with faster response to disturbances for precision position keeping. In: 2014 IEEE International Symposium on Safety, Security, and Rescue Robotics (2014), pp. 1–5, Hokkaido, Japan (2014). https://doi.org/10.1109/SSRR.2014.7017669

13. Voyles, R., Jiang, G.: Hexrotor uav platform enabling dextrous interaction with structures - preliminary work. In: 2012 IEEE International Symposium on Safety, Security, and Rescue Robotics (SSRR), pp. 1–7, College Station, TX, USA (2012). https://doi.org/10.1109/SSRR.2012.6523891

14. Crowther, B., Lanzon, A., Maya-Gonzalez, M., Langkamp, D.: Kinematic analysis and control design for a nonplanar multirotor vehicle. J. Guid. Control Dyn. **34**(4), 1157–1171 (2011). https://doi.org/10.2514/1.51186

15. Rajappa, S., Ryll, M., Bulthoff, H.H., Franchi, A.: Modeling, control and design optimization for a fully-actuated hexarotor aerial vehicle with tilted propellers. In: 2015 IEEE International Conference on Robotics and Automation (ICRA), pp. 4006–4013, Seattle, WA, USA (2015). https://doi.org/10.1109/ICRA.2015.7139759

16. Ryll, M., Muscio, G., Pierri, F., Cataldi, E., Antonelli, G., Caccavale, F.: Franchi, A.: 6d physical interaction with a fully actuated aerial robot. In: 2017 IEEE International Conference on Robotics and Automation (ICRA), pp. 5190–5195, Singapore, Singapore (2017). https://doi.org/10.1109/ICRA.2017.7989608

17. Park, S., Her, J., Kim, J., Lee, D.: Design, modeling and control of omni-directional aerial robot. In: 2016 IEEE/RSJ International Conference on Intelligent Robots and Systems (IROS), pp. 1570–1575, Daejeon, South Korea (2016). https://doi.org/10.1109/IROS.2016.7759254

18. Nikou, A., Gavridis, G.C., Kyriakopoulos, K.J.: Mechanical design, modelling and control of a novel aerial manipulator. In: 2015 IEEE International Conference on Robotics and Automation (ICRA), pp. 4698–4703, Seattle, WA, USA (2015). https://doi.org/10.1109/ICRA.2015.7139851

19. Brescianini, D., D'Andrea, R.: Design, modeling and control of an omni-directional aerial vehicle. In: 2016 IEEE International Conference on Robotics and Automation (ICRA), pp. 3261–3266, Stockholm, Sweden (2016). https://doi.org/10.1109/ICRA.2016.7487497

20. Roque, P., Ventura, R.: Space cobot: Modular design of an holonomic aerial robot for indoor microgravity environments. In: 2016 IEEE/RSJ International Conference on Intelligent Robots and Systems (IROS), pp. 4383–4390, Daejeon, South Korea (2016). https://doi.org/10.1109/IROS.2016.7759645

21. Zhao, M., Anzai, T., Shi, F., Chen, X., Okada, K., Inaba, M.: Design, modeling, and control of an aerial robot dragon: A dual-rotor-embedded multilink robot with the ability of multi-degree-of-freedom aerial transformation. IEEE Robot. Autom. Lett. **3**(2), 1176–1183 (2018). https://doi.org/10.1109/LRA.2018.2793344

22. Ramp, M., Papadopoulos, E.: Attitude and angular velocity tracking for a rigid body using geometric methods on the two-sphere. In: 2015 European Control Conference (ECC), pp. 3238–3243, Linz, Austria (2015). https://doi.org/10.1109/ECC.2015.7331033

23. Ramp, M., Papadopoulos, E.: On modeling and control of a holonomic vectoring tricopter. In: 2015 IEEE/RSJ International Conference on Intelligent Robots and Systems (IROS), pp. 662–668, Hamburg, Germany (2015). https://doi.org/10.1109/IROS.2015.7353443

24. Tayebi, A., McGilvray, S.: Attitude stabilization of a vtol quadrotor aircraft. IEEE Trans. Control Syst. Technol. **14**(3), 562–571 (2006). https://doi.org/10.1109/TCST.2006.872519

25. Lee, T., Leok, M., Harris McClamroch, N.: Control of complex maneuvers for a quadrotor uav using geometric methods on se(3). arXiv:1003.2005, arXiv:1003.2005v1 (2010)

26. Fossen, T.: Handbook of Marine Craft Hydrodynamics and Motion Control. John Wiley & Sons Ltd. https://doi.org/10.1002/9781119994138 (2011)

27. Ramp, M., Papadopoulos, E.: On the global behavior of a geometric PDAV controller by means of a geometrically exact linearization. J. Dyn. Syst. Meas. Control **143**(7). https://doi.org/10.1115/1.4049552 (2021)

28. Goldstein, H., Poole, C., Safko, J.: Classical Mechanics, 3 edn. Addison-Wesley (2001)

29. Chaturvedi, N.A., Sanyal, A.K., McClamroch, N.H.: Rigid-body attitude control. IEEE Control. Syst. **31**(3), 30–51 (2011). https://doi.org/10.1109/MCS.2011.940459

30. Lee, T.: Geometric tracking control of the attitude dynamics of a rigid body on so(3). In: Proceedings of the 2011 American Control Conference, pp. 1200–1205, San Francisco, CA, USA (2011). https://doi.org/10.1109/ACC.2011.5990858

31. Bhat, S.S., Bernstein, D.: A topological obstruction to continuous global stabilization of rotational motion and the unwinding phenomenon. Syst. Control Lett. **39**(1), 63–70 (2000). https://doi.org/10.1016/S0167-6911(99)00090-0

32. Crassidis, J., Markley, L.: Unscented filtering for spacecraft attitude estimation. In: Journal of Guidance Control and Dynamics, vol. 26 (2003). https://doi.org/10.2514/2.5102

33. ANALOG DEVICES: ADIS16477 Precision, Miniature MEMs IMU. https://www.analog.com/media/en/technical-documentation/data-sheets/ADIS16477.pdf. Datasheet, 5/2019 — Rev. C (2019)

34. Nousias, S., Papadopoulos, E.: Quadruped robot roll and pitch estimation using an unscented kalman filter. In: 2016 24th Mediterranean Conference on Control and Automation (MED), pp. 731–736, Athens, Greece (2016). https://doi.org/10.1109/MED.2016.7535894

35. Robotis: XL430-W250 DYNAMIXEL Position Sensor e-manual. http://emanual.robotis.com/docs/en/dxl/x/xl430-w250/. Datasheet (Released on 2018, 3rd quarter) (2018)

36. Batchelor, G.: An Introduction to Fluid Dynamics. Cambridge Mathematical Library. Cambridge University Press. https://books.google.gr/books?id=aXQgAwAAQBAJ (2000)

37. Mellinger, D., Kumar, V.: Minimum snap trajectory generation and control for quadrotors. In: 2011 IEEE International Conference on Robotics and Automation, pp. 2520–2525, Shanghai, China (2011). https://doi.org/10.1109/ICRA.2011.5980409

38. Bullo, F., Lewis, A.: Geometric Control of Mechanical Systems, Texts in Applied Mathematics, vol. 49. Springer New York (2004)

Michalis Ramp received his Diploma in Mechanical Engineering (ME) from the University of Cyprus, in 2008. He was a recipient of the Fulbright scholarship award for MS studies in the USA, where he obtained his master's in ME from the University of California at Berkeley, in 2010. Currently he is a Ph.D. candidate with the Department of Mechanical Engineering at NTUA (supervisor Professor Evangelos Papadopoulos). His current research interests include modeling of dynamic systems, robotics (with a special interest in Unmanned Aerial Systems (UAS)), nonlinear control systems, geometric mechanics/control, and applied mathematics. He is a member of the NTUA Control Systems Lab (CSL), of the Cyprus Scientific and Technical Chamber (ETEK), and of the Cyprus Mechanical Engineering Association (CMEA).

Evangelos Papadopoulos received a Diploma from NTUA (1981), Greece, and subsequently a MS (1983) and a PhD (1991) degree from MIT, all in Mechanical Engineering. In 1991 he was appointed a Lecturer at MIT and joined McGill University as an Assistant Professor. Since 1997 he is a Professor of Mechanical Engineering at NTUA. He teaches courses in Robotics, Controls, Mechatronics, Circuits, and Electromechanical Systems. He serves as an Associate Editor of the *Mechanism and Machine Theory*, and of the *Frontiers in Space Robotics*. He conducts research in robotics, including space robotics, biomimetic robots, microrobotics, mechatronics, haptic devices, simulators, and applied control, with funding from the EU (Horizon), ESA, private, and national sources. He is author or co-author of more than 350 technical papers, and the author of three books in Greek. Dr. Papadopoulos is a Fellow of IEEE, a Fellow of ASME, an Associate Fellow of AIAA, and a member of Sigma Xi, and the Technical Chamber of Greece.